POLITECNICO
MILANO 1863

SCUOLA DI INGEGNERIA INDUSTRIALE
E DELL'INFORMAZIONE

ASTEROID EJECTA CAPTURE AROUND BINARY SYSTEMS: APPLICATION TO THE DART MISSION

Tesi di Laurea Magistrale in
Space Engineering - Ingegneria Spaziale

Author: **Francesco Ventre**

Student ID: 915940
Advisor: Prof. Francesco Topputo
Co-advisors: Prof. Stefania Soldini, Dr. Fabio Ferrari
Academic Year: 2021-22

Ai miei nonni
Biagio, Rosa,
Francesco ed Antonietta

Abstract

Investigation of the post-impact fate of the ejecta clouds generated by the impact on asteroids is a crucial element to plan kinetic impactor missions and understanding planetary formation mechanisms.
In particular, the Asteroid Impact and Deflection Assessment (AIDA) mission is a joint effort between ESA and NASA to the near-Earth binary asteroid (65803) Didymos, whose objective is to impact a first spacecraft (DART) on the smaller body of the binary in the October 2022 and, with the following HERA mission in 2027, assessing the deflection as a consequence of the kinetic impact. The mission is intended to offer insights into the Solar System formation and into the deflection techniques to be employed to protect the Earth from Potentially Hazardous Asteroids.
The purpose of this thesis is to assess the fate of the ejecta cloud around the binary system due to the impact of DART, by investigating the energy level of the particles involved.
As the dynamics around asteroids is well known to be challenging due to the gravity field generated by their irregular mass distribution, in this work are discussed different representation of the gravity field, and the most suitable are selected to correctly simulate the forces environment. Also, the Scaling Laws model used for the ejecta initialization is presented and discussed.
The energy level study is conducted in the context of the Augmented Hill Problem, a particular three-body problem that considers a very small secondary and the Solar Radiation Pressure effect on the motion. Such a model is extensively characterized in this work for the Didymos system.
A set of particles with different diameters is generated, constraining their velocity according to the Scaling Laws, such to focus on particles that are less likely to escape right after the impact. After propagating the particles for 6 hours, their energy level is compared with the one associated with the equilibrium point L_2 of the Augmented Hill Problem, with the purpose of investigating the particles' fate.

Keywords: Binary Asteroid; Ejecta Dynamics; Gravitational Model; Asteroid Dynamics;

Sommario

Effettuare indagini riguardo l'evoluzione delle nubi di particelle create a valle di un impatto con asteroidi è un elemento cruciale per pianificare missioni che prevedono l'impatto di una sonda con un corpo celeste e per comprendere i meccanismi di formazione planetaria. In particolare, la missione Asteroid Impact and Deflection Assessment (AIDA) è una missione congiunta ESA/NASA diretta verso l'asteroide binario vicino alla Terra (65803) Didymos, il cui obiettivo è quello di impattare un veicolo spaziale (DART) sul corpo più piccolo del sistema binario nell'Ottobre del 2022 ed, in seguito, con la missione HERA pianificata per il 2027, valutare la variazione orbitale subita dal corpo. La missione AIDA si propone di investigare riguardo la formazione del Sistema Solare e le tecniche da impiegare per proteggere la Terra da asteroidi potenzialmente pericolosi.
Scopo di questa tesi è valutare l'evoluzione della nube di ejecta nei pressi del sistema binario causata dall'impatto di DART, studiando il livello di energia delle particelle coinvolte. Essendo nota la complessità della dinamica in prossimità di asteroidi a causa del campo gravitazionale generato dalla loro irregolare distribuzione di massa, in questo lavoro vengono discussi i problemi relativi alla diversa rappresentazione del campo gravitazionale, selezionando i modelli più adatti a simulare correttamente le forze coivolte. Inoltre, viene presentato e discusso il modello delle "Scaling Laws" utilizzato per l'inizializzazione delle particelle.
Lo studio del livello energetico viene condotto nel contesto dell'Augmented Hill Problem, un particolare problema ai tre corpi che considera un corpo secondario molto piccolo e l'effetto della Pressione di Radiazione Solare sul moto. Tale modello è qui ampiamente caratterizzato per il sistema Didymos.
In questo studio è generato un insieme di particelle con diametri differenti, vincolandone la velocità secondo le già menzionate Scaling Laws, così da investigare particelle che hanno meno probabilità di sfuggire la gravità del sistema binario appena dopo l'impatto.
Dopo aver propagato le particelle per 6 ore, il loro livello di energia è confrontato con quello associato al punto di equilibrio L_2 nel problema di Hill, allo scopo di indagare la loro evoluzione nel tempo.

Parole chiave: Asteroidi binari, dinamica delle polveri, modelli gravitazionali, dinamica intorno agli asteroidi,

Ringraziamenti

In direzione ostinata e contraria. È così che mi piace definire il mio percorso, che non è stato assolutamente semplice. E non intendo solo la mia carriera accademica, quanto tutti i sentieri tortuosi che ho percorso per dover arrivare a questo punto, partendo da un piccolo paesino di provincia e da una situazione economica non sempre stabile.
Non sono, né sarò l'unico, ma ecco, è il momento giusto per me di guardarmi alle spalle e celebrare anni di sacrifici, di crescita personale e duro lavoro.
Sono sempre stato del parere che nessuno possa salvarsi da solo, e che nella vita ci sia necessità costante di sognare in grande, ispirarsi ed ispirare. Spero e credo di averlo fatto, e riconosco di aver avuto la fortuna di incontrare compagni di viaggio eccezionali che desidero ringraziare qui.

Un primo, fondamentale ringraziamento va ai miei genitori. Mi hanno introdotto alla conoscenza, mi hanno permesso di crescere liberamente, fare le mie scelte, i miei errori, e di questo non potrò mai ringraziarli abbastanza. Così come non potrò mai ripagare il supporto economico che mi hanno dato finora e che non mi hanno mai fatto pesare.

Ringrazio mio fratello, Roberto. Un pilastro della mia vita sempre presente in ogni situazione. Generoso, apprensivo, volenteroso. Quando tutto sembrava crollare, pensando a te potevo ritrovare me stesso. Sappi che mi hai aiutato moltissimo, anche se non lo do a vedere.

Ringrazio i miei nonni, ai quali questa tesi è dedicata. Grazie per avermi dato la vita e per tutto l'affetto che non è mai mancato. Grazie anche a te nonno Biagio, perché so che mi guardi sempre, dovunque tu sia, e che mi hai dato tante volte la forza di non mollare.

Grazie ai miei amici dei Minority: Sebastiano, Stany, Saverio, Jacopo e Pietro. Il vostro supporto non è mai mancato in tutto questo tempo, ed ho sempre letto nei vostri occhi una fiducia straordinaria nelle mie capacità. Avere degli amici come voi rende tutto migliore. Grazie anche per tutte le avventure, con l'auspicio di poterne vivere ancora molte.

Ringrazio il Team Ringo Goal (Alfonso, Francesco, Valerio, Marco e Luigi) per il supporto costante, le risate, le esperienze trascorse insieme e l'affetto che ci lega dal liceo. Un particolare ringraziamento va a Luigi ed Alfonso, che spesso mi sono stati vicino in momenti particolari.

A Daniele, Americo, Geremia, Luca ed Andrea dico grazie, per aver condiviso con me

momenti bellissimi, per l'aiuto tecnologico che tutti vorrebbero, per l'incoraggiamento a non mollare mai.

Ringrazio moltissimo Camilla, spesso unica persona a capirmi in momenti davvero difficili. Non basterà una vita per ringraziarti per tutto il supporto che mi hai dato in questi anni, ma sai che sarò sempre al tuo fianco, quando e come vorrai.

Ringrazio tutti gli amici di "Friends", che da quando sono a Milano non mi hanno mai fatto sentire solo. Aver trovato voi ad accogliermi è stato molto bello. Grazie per i momenti spensierati vissuti insieme.

Un ringraziamento speciale ai miei colleghi di università, in particolare ad Andrea, Carmine, Nicola S., Nicola B., Simone, Limo e Tarone, i quali hanno camminato per più tempo al mio fianco. Anche voi mi avete dato una spinta immensa per poter arrivare fin qui, e di questo vi sarò sempre grato. Grazie a Salvatore e Marzio, sinceri ed affettuosi amici che spero di non perdere.

Grazie ad Elisa. Non trovo neanche le parole per esprimere la mia gratitudine. Dai progetti insieme a tutte le volte che ci siamo confrontati ed abbiamo sclerato. Grazie per quella volta che ti ho chiamata per far parte di PoliSpace e tu ci sei stata, grazie per la tua presenza e... Per tutto il resto.

Ringrazio i colleghi di Walle Mobility per avermi dato l'opportunità di maturare ed accrescere le mie competenze nell'ambito business e startup. La mia vita sarebbe stata diversa senza questa avventura cominciata insieme. Grazie Alessandro, Andrea, Carmine, Marco, Giorgio, Guido e Vincenzo.

Ringrazio il professore Topputo e il dottor Fabio Ferrari, per avermi dato l'opportunità di intraprendere questo percorso di tesi. Un ringraziamento speciale alla professoressa Soldini per il supporto e la disponibilità nella supervisione del mio lavoro.

Un grazie immenso a tutti i ragazzi di PoliSpace, in particolare a Swarnajyoti ed Aloisia. Grazie per aver creduto in me ed avermi supportato, sempre. Il nostro sostegno reciproco ci ha portato lontano. Siete due persone (prima che ingegneri) eccezionali.

Grazie, dicevo, a quelli che hanno cominciato con me l'avventura della prima associazione spaziale del Politecnico ed a tutti quelli che verranno, con l'augurio che possiate realizzare grandi cose.
Ho dato tanto per l'associazione, specialmente il mio tempo. Ad oggi, sono fiero dei traguardi raggiunti e spero possa continuare così. Inoltre, sono orgoglioso di essere stato il vostro presidente, mi avete insegnato tanto sia come leader che come persona e non vi dimenticherò mai.

Je ne regrette rien. Alatis grave nihil.

Contents

1 Introduction

The history of space exploration started a long time ago, when humankind was observing the sky, being fascinated by the stars. As it is well known, the perseverance of these observations led to the discovery of the solar system, its planets, and of a plethora of small objects with peculiar characteristics such as asteroids, comets and cosmic dusts. The importance of studying these objects in detail by intercepting them with probes, realizing a space laboratory and possibly returning back some samples, became clear and especially feasible at the beginning of the 80's, when several spacecrafts were aimed to intercept the *Halley Comet*, creating the so-called "Halley armada". [1]

An historical overview on the asteroids and comet missions performed since then is reported in section 1.1, with a particular emphasis on the mission of interest for this thesis, the Asteroid Impact and Deflection Assessment (AIDA) mission to binary asteroid *65803 Didymos* [2].

Asteroids are typically small-sized, which implies the exertion of small gravitational forces. Therefore, objects orbiting such celestial bodies are severely affected even by small perturbations. The dynamical environment is in turn challenging to study for operating and designing space missions. Due to the reasons stated above, the design and study of these missions is a flourishing area, and expected to become increasingly prominent in the coming years.

The motivation beyond this thesis is related to a specific field of asteroid mission design that include an impactor: the assessment of the dynamical evolution of ejecta particles. Such a motion is considered of interest because, apart from the information that can offer about the emitting body's characteristics, it can give insights on the processes that gave birth to our solar system.

Although several studies about the ejecta fate have been performed in the past years, [3, 4] including some with a focus on the AIDA mission [5, 6], the purpose of this thesis is to evaluate their evolution from the assessment of their energy level (i.e. Jacobi constant) in the context of the Augmented Hill Problem.

The rationale behind this work and an overview of its contents are reported respectively in section 1.2 and section 1.3.

1.1. Historical review

Since the early 80's an international effort have been posed to inquire from a close distance minor bodies of the solar system, such as comets and asteroids.
Some missions, after the accomplishment of their primary objective, were therefore redirected towards minor bodies. It's the case of the International Cometary Explorer (ICE) mission (NASA/ESA), first mission to fly past a comet, targeting the *21P/Giacobini-Zinner* [7] and Vega 1 and 2 (USSR), intercepting the *Halley Comet* [8]. The latter mission and others paved the way for Giotto (ESA), the first deep space mission from the European Space Agency, achieving a 600 km flyby with the *Halley Comet* in 1986. [9]
The beginning of the 90's saw instead the first human made object flying past an asteroid, with the Galileo probe (ESA) intercepting *951 Gaspra* and *243 Ida* on its way to Jupiter. [10] The very first mission to target an asteroid (*433 Eros*) was indeed Near Earth Asteroid Rendezvous (NEAR) Shoemaker (NASA), whose spacecraft became the first human-made object to orbit a minor body in February 2000. [11]
In the following years efforts were put towards landing and/or return of samples from deep space. That was the case of Japan Aerospace eXploration Agency (JAXA)'s mission Hayabusa, capable of returning samples from the asteroid *25143 Itokawa* in 2005 [12], Stardust (NASA), that returned to Earth samples of the coma of comet *81-P Wild* in January 2006 [13] and Rosetta (ESA) , first spacecraft to orbit a cometary nucleus (*67P/ Churyumov-Gerasimenko*) and to visit the surface through a lander, in 2014 [14]. Remarkable sample return missions towards Near-Earth Asteroids (NEAs) performed in more recent years are Hayabusa 2 (JAXA) to asteroid *162173 Ryugu*, that successfully returned samples to Earth in 2020 [15] and OSIRIS-REx (NASA) that touched down asteroid *101955 Bennu* in the same year and is expected to return samples in 2023 [16]. Several exploration and sample return missions to minor bodies are ongoing or planned in the coming years, such as Lucy (NASA), launched at the end of 2021 to explore Trojan asteroids [17], Zheng He (CNSA) a sample return mission to asteroid *69219 Kamo'oalewa* scheduled for launch in 2024 [18] and Destiny+ (JAXA) a technology demonstration mission to collect dust from the active asteroid *3200 Phaethon* in 2028. [19]

1.1.1. Binary NEAs: a planetary defense opportunity

As seen, in the last decades, due to their large accessibility to spacecrafts, NEAs have become the target of several deep space missions. NEAs are a sub-category of the so-called Near-Earth objects (NEOs), classified with respect to their semi-major axis (a), perihelion distance (q), aphelion distance (Q) and absolute magnitude (H) (see Table 1.1 for details). NEOs are defined as "all small Solar System bodies with orbits around the Sun that lie partly between 0.983 and 1.3 AU away from the Sun". [20] In particular, NEAs are asteroids with a perihelion distance less than 1.3 AU and an aphelion distance of approximately 1 AU. At the time being, their population is estimated to be of more

than 28500 unities.
If their Minimum Orbit Intersection Distance (MOID) with the Earth overcomes a certain threshold, these asteroids are considered as Potentially Hazardous Asteroids (PHAs), meaning that they are large enough to cause significant regional damage in the event of impact.

Group	Definition	Description
NECs	*q<1.3 au* *P<200 years*	Near-Earth Comets
NEAs	*q<1.3 au*	Near-Earth Asteroids
Atiras	*a<1.0 au* *Q<0.983 au*	NEAs whose orbits are contained entirely with the orbit of the Earth (named after asteroid 163693 Atira).
Atens	*a<1.0 au* *Q>0.983 au*	Earth-crossing NEAs with semi-major axes smaller than Earth's (named after asteroid 2062 Aten).
Apollos	*a>1.0 au* *q<1.017 au*	Earth-crossing NEAs with semi-major axes larger than Earth's (named after asteroid 1862 Apollo).
Amors	*a>1.0 au* *1.017<q<1.3 au*	Earth-approaching NEAs with orbits exterior to Earth's but interior to Mars' (named after asteroid 1221 Amor).
PHAs	*MOID<=0.05 au* *H<=22.0*	Potentially Hazardous Asteroids

Table 1.1: Near-Earth Objects classification. NEAs are divided into four groups (Atiras, Atens, Apollos, Amor) based on their semi-major axis (a), perihelion distance (q), aphelion distance (Q) and Absolute Magnitude(H).

As of February 2022, about the 12.5% of the NEAs population is known to represent a threat to Earth. [21]
Since 1993, when the Galileo spacecraft imaged the asteroid moon *Dactyl* while performing a flyby near its bigger companion *243 Ida* [22], binary asteroids started gaining interest in the scientific community. In the last few decades, many multiple asteroid systems were discovered [23] (see Table 1.3) and it is currently estimated that about 16% of NEAs are binaries. [24] As of February 2022, there are 459 minor planets with companion for a total of 479 known companions, including triple, quadruple and other systems. A list of the number of objects divided per location in the solar system [25] is reported in Table 1.2

# of Systems	Orbital class
80	Near-Earth objects
31	Mars-crossing asteroids
193	Main-belt asteroids
6	Jupiter trojans
2	Centaurs
114	Trans-Neptunian objects

Table 1.2: Number of minor planets with companions (not only binaries) per Solar System region

The threat represented by these asteroids have inspired space missions aimed to defend our planet in several ways.
It is the case of NEOWISE, a NASA infrared-wavelength astronomical space telescope currently identifying and characterizing the population of NEOs [26], the Asteroid Redirect

System					Primary			Secondary			
Designation	Class	D (km)	s/p	YOD	D (km)	RT (h)	YOD	D (km)	RT (h)	as (km)	Ps (h)
1862 Apollo	APO	1.55	0.052	1932	1.55	3.065	2005	0.08	–	3.75	27.36
1866 Sisyphus	APO	8.48	0.1	1972	8.44	2.3909	1985	0.84	–	19	27.12
3671 Dionysus	AMO	1.46	0.2	1984	1.43	2.705	1997	0.29	–	3.4	27.744
5143 Heracles	APO	3.65	0.167	1991	3.6	2.706	2011	0.6	–	4	15.5
5381 Sekhmet	ATE	1.04	0.3	1991	1	2.7	2003	0.3	10	1.54	12.5
7088 Ishtar	AMO	1.51	0.42	1992	1.39	2.679	2006	0.33	–	2.8	20.6496
15745 Yuliya	AMO	1.2	0.46+	1991	0.61+	3.2495	2018	0.28+	–	–	11.735
65803 Didymos	AMO	0.77	0.22	1996	0.75	2.259	2003	0.17	–	1.18	11.8992
66391 Moshup	ATE	1.39	0.341	1999	1.317	2.7645	2001	0.451	17.4	2.548	17.4216
69230 Hermes	APO	0.81	0.9	1937	0.6	13.894	2003	0.54	13.892	1.1	13.8936
163693 Atira	ATI	4.9	0.21	2003	4.8	2.9745	2017	1	–	6	15.504

Table 1.3: List of some NEAs with companions. Class is the abbreviation of Amor, Apollo, Atira and Athens. D is the diameter in km, s/p is the secondary-to-primary ratio. YOD is the year of discovery. RT is the rotation time in hours, as and Ps are respectively the semi-major axis (km) and the revolution period of the secondary (hours). [25]

Mission (ARM), aimed to collect a massive boulder from a NEA, now cancelled [27, 28] or the NEA Scout, a solar-sail propelled CubeSat to be deployed during the Artemis I mission to inquire about NEAs features. [29]

A good opportunity to set up a planetary defense mission in scale has been found in binary asteroids. Asteroid Impact and Deflection Assessment (AIDA) mission, a joint effort between ESA and NASA is in fact aimed to assess the deflection of the secondary of the binary system *(65803) Didymos* as a consequence of a kinetic impact. [2] The AIDA mission architecture includes two spacecraft, designed independently by ESA and NASA. The European contribution is called Asteroid Impact Mission (AIM) (now HERA), while the US one Double Asteroid Redirection Test (DART). [30] The latter, launched in November 2021, is expected to impact the smaller body of the Didymos binary ("Didymos B" or "Didymoon") in October 2022, releasing a CubeSat (LiciaCUBE) [31] to take images of the event and leave the system shortly. The HERA spacecraft is scheduled to depart in 2024 to reach the binary system in 2027 and investigate the impact effects. [32] It will release two small satellites: Juventas, a 6U CubeSat responsible of observing the moon of the system from a few km, while operating fully autonomously using the Hera mothercraft as a proxy [33] and Milani, another 6U CubeSat aimed to map the binary bodies and determine the composition of the ejecta created after the impact [34] .

1.2. Motivation and research question

The ejecta generated from small bodies is a consequence of processes that activate and modify the surface of the bodies themselves. Such cloud of particles can represent an hazard for missions coming after the release of material.

Especially, in the context of the AIDA mission, the presence of a second spacecraft aimed to the asteroid and of CubeSats in support of the main mission, makes necessary a precise assessment of the ejecta fate about Didymos.

The objective of this thesis is to infer on the evolution of the ejecta particles generated by the impact of DART on the smaller body of the binary asteroid system (65803) Didymos using a high fidelity model, and by evaluating their energy level, using a different approach from the studies carried on up to date.
Given all the previous considerations, the main question this thesis wants to answer is:

How will the ejecta produced from the DART impact evolve?

This main research question is broken into three objectives of study as follows:

What is the dynamical environment for a third body orbiting in proximity of the Didymos system?

This implies studying the dynamical environment around the binary asteroid in a high fidelity model to examine the forces acting on the third body and the order of magnitude of the perturbations. The comparison of different strategies for the design of the irregular gravity field is performed to find the optimum for the analysis.

Which is the best model to simulate the particles ejection following the impact of DART?

The ejecta modelling state of the art is reported and detailed. The quantities of interest for this study are computed by means of the appropriate model.

What is the post-impact ejecta fate with respect to their energy level in the context of the Augmented Hill Problem?

This task is accomplished by propagating the particles generated through the Scaling Laws for a certain time after the impact, and then comparing their energy level with a reference value (the L_2 equilibrium point energy) in the context of the Augmented Hill Problem.

1.3. Thesis overview

This work is divided in three main chapters. The first one (chapter 2) is intended to offer detailed information about the theoretical background needed. It contains explanation of the main gravitational models for small bodies, a description of the Augmented Hill Problem and the analytic condition for a particle to be bounded to an asteroid in the same context. Moreover, in the same chapter are characterized the so-called "Scaling Laws", to serve as a model for the ejecta particles initialization.
In chapter 3, are instead described the dynamical models employed along with the reference frames involved. A model of the Didymos system in the context of the Augmented Hill

Problem is also discussed, and at the end of the chapter the process of ejecta initialization is reported.
In chapter 4 are reported all the details regarding the simulation along with the results retrieved and, finally, in chapter 5 the outcomes of this work are summarized, offering perspectives on the potential future developments. Notice that a verification of all the models employed in this work is reported in Appendix A.

2 | Theoretical Background

Modeling the dynamics around binaries is a very challenging task, as several effects have to be taken into account: mutual rotation of the bodies around each other, rotational motion, shapes and relevant perturbations. In this work is also considered the formulation of a peculiar three-body problem, namely Augmented Hill Problem, to retrieve the energy level that will lead to the final considerations. Additionally, a proper model for the ejecta generation is adopted to accurately simulate their size and initial conditions.
In this section is reported all the theoretical framework used to build up the models adopted. Available formulations for the gravity of small bodies are included in section 2.1, an overview on the Augmented Hill problem can be found in section 2.2 and finally, a description of the model adopted for the impact (i.e. the ejecta generation) is described in section 2.3. For the sake of completeness, the validation of the models used in this work is reported in Appendix A.

2.1. Small bodies gravitational models

Main dynamical models for the gravity field around small bodies are: Triaxial Ellipsoid, Spherical Harmonics Expansion, Polyhedral gravity field and Mass concentration (Mascon) model. [35]
Advantages and disadvantages of each method are summarized in Table 2.1.

Gravity Model	Pros	Cons
Triaxial Ellipsoid	- Simple to implement - Good first approx.	
Spherical Harmonics Expansion	- Approaches exact gravity as the order increases - Low computational cost - Poorly affected by the level of accuracy - Useful for long simulations model	- Variable model complexity - Valid only outside of the Brillouin's sphere
Mascons	- Depends on the masses' distribution strategy - Can deal with any shape and density variation - Provides gravity values inside the Brillouin sphere	- High computational cost - Constant density hypothesis
Polyhedral	- Can deal with any shape (homogeneous) - Gravity field preserved up to the body's surface - Laplacian to check the position wrt body	- High computational cost - Density must be constant

Table 2.1: Pros and cons of the main gravity field models around small bodies

In the following subsections an overview on each of the mentioned models is reported to justify the choices made in this work.

2.1.1. Triaxial Ellipsoid

The Triaxial Ellipsoid constitutes a good (first) approximation for objects with one major elongated axis (and constant density). [36]

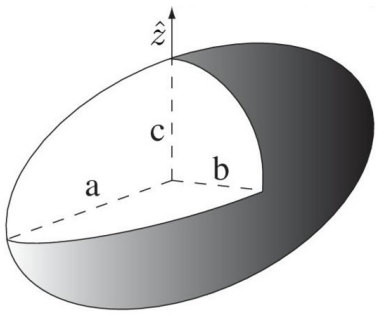

Fig. 2.1: Schematic of a triaxial ellipsoid shape

Considering an object with $a > b > c$ (see Figure 2.1), the formula to compute the potential for is Equation 2.1.1:

$$\begin{aligned} U = \frac{G\rho 2\pi abc}{\sqrt{a^2-c^2}} \Bigg\{ & \left[1 - \frac{x^2}{a^2-b^2} + \frac{y^2}{a^2-b^2}\right] F\left(\omega_\kappa, k\right) + \\ & + \left[\frac{x^2}{a^2-b^2} - \frac{\left(a^2-c^2\right)y^2}{\left(a^2-b^2\right)\left(b^2-c^2\right)} + \frac{z^2}{b^2-c^2}\right] E\left(\omega_\kappa, k\right) + \\ & + \left[\frac{c^2+\kappa}{b^2-c^2}y^2 - \frac{b^2+\kappa}{b^2-c^2}z^2\right] \frac{\sqrt{a^2-c^2}}{\sqrt{\left(a^2+\kappa\right)\left(b^2+\kappa\right)\left(c^2+\kappa\right)}} \Bigg\} \end{aligned} \tag{2.1.1}$$

Where κ is the highest root of the equation:

$$\frac{x^2}{a^2+\kappa} + \frac{y^2}{b^2+\kappa} + \frac{z^2}{c^2+\kappa} = 1 \tag{2.1.2}$$

And also,

$$k = \frac{a^2-b^2}{a^2-c^2}; \qquad sin(\omega_k) = \sqrt{\frac{a^2-c^2}{a^2+\kappa}} \tag{2.1.3}$$

F, E are Legendre's integrals respectively of the first and second kind, that have expression:

$$F\left(\omega_\kappa, k\right) = \int_0^{\omega_\kappa} \frac{d\varphi}{\sqrt{1-k^2\sin^2(\varphi)}} \tag{2.1.4}$$

$$E\left(\omega_\kappa, k\right) = \int_0^{\omega_\kappa} \sqrt{1-k^2\sin^2(\varphi)}d\varphi \tag{2.1.5}$$

2.1.2. Spherical Harmonics Expansion

The exterior/interior gravity field expression is one of spherical harmonic expansions of the gravity field, which is obtained by solving Laplace's equation by separation of variables [37]. In fact, the separation of variables yield two solutions for Laplace's equation: internal and external.
The most widely used gravitational potential expression is the exterior gravity field in Equation 2.1.6:

$$U^e = \frac{GM^*}{R_e^*} \sum_{n=0}^{\infty} \sum_{m=0}^{n} \left(\frac{R_e^*}{r} \right)^{n+1} P_{nm}(\sin\phi) \begin{bmatrix} \cos(m\lambda) \\ \sin(m\lambda) \end{bmatrix} \begin{bmatrix} C_{nm}^e \\ S_{nm}^e \end{bmatrix} \tag{2.1.6}$$

where U is the potential, e super/subscript denote the exterior quantity, G is the gravitational constant, M^* is the reference mass (nominally the total mass of the body), R^* is the reference radius (nominally the radius of the Brillouin sphere), r is the spacecraft position, P_{nm} is the associated Legendre function of degree n and order m, C_{nm} and S_{nm} are spherical harmonic coefficients, λ is longitude, and ϕ is latitude in the body-fixed frame. This exterior gravity field, as described in detail by [38], is generally valid only outside the circumscribing sphere of an asteroid, hence the name "exterior gravity field". Such sphere is also called the Brillouin sphere, within which all mass elements of the asteroid reside [39]. Thus, for general body shapes, the exterior gravity field does not model the dynamical environment within the Brillouin sphere, which poses a problem when performing proximity operations around asteroids. The exterior gravity field expression is one of spherical harmonic expansions of the gravity field, which is obtained by solving Laplace's equation by separation of variables as mentioned above. In fact, the separation of variables yield two solutions for Laplace's equation, the other type of which is referred to as the interior gravity field Equation 2.1.7:

$$U^i = \frac{GM^*}{R_e^*} \sum_{n=0}^{\infty} \sum_{m=0}^{n} \left(\frac{r}{R_i^*} \right)^{n} P_{nm}(\sin\phi) \begin{bmatrix} \cos(m\lambda) \\ \sin(m\lambda) \end{bmatrix} \begin{bmatrix} C_{nm}^i \\ S_{nm}^i \end{bmatrix} \tag{2.1.7}$$

This interior gravity field converges interior to the Brillouin sphere and outside of the body. The convergence region of the interior gravity field is up to a point on the surface where the interior Brillouin sphere makes a contact, as shown in Figure 2.2
It is therefore apparent that a major drawback of the interior gravity field is that many of them are necessary to map out the entire space of the gravity field around the body (i.e., total mapping). This problem becomes more critical when is required to map out the gravity field in a severely concave region, which is a prominent feature of contact binaries. In contrast, the interior gravity field is shown to be accurate for regional mapping where the surface is smooth.

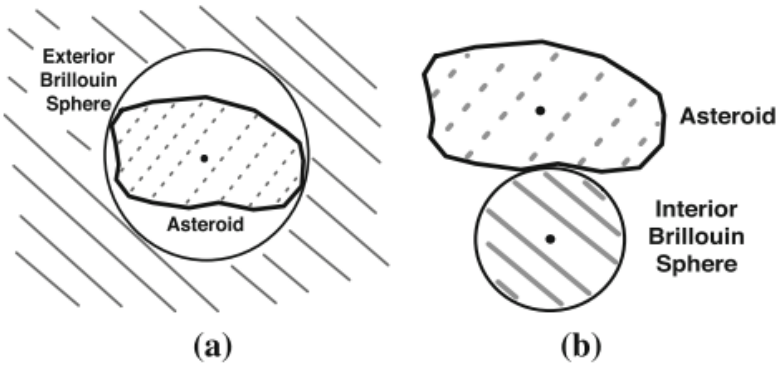

Fig. 2.2: Schematic of the external and internal Brillouin sphere for a generic shaped asteroid

2.1.3. Polyhedral Gravity Field

The polyhedral gravity field (i.e., the shape model gravity field [40, 41]) consists in modeling the asteroid as a constant-density polyhedron. By polyhedron it is meant a three-dimensional solid body whose surface consists of planar faces meeting along straight edges or at isolated points called vertices. Exactly two faces meet at each edge. Three or more edges and a like number of faces meet at each vertex. As the vertex coordinates of a polyhedron alone are insufficient to describe it, the connective topology must also be described - edges connect which vertex pairs and bound which face pairs (see Figure 2.3 and Figure 2.4)

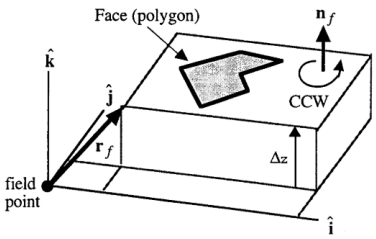

Fig. 2.3: Each polyhedron face has its own Cartesian coordinate system oriented so that k is aligned with the face's normal vector $\hat{\boldsymbol{n}}_f$. Vector $\mathbf{r}_f$ extends from the field point to any point in the face plane. Courtesy of [41]

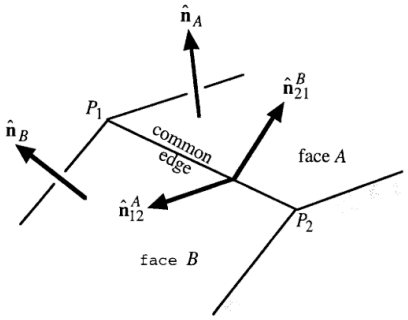

Fig. 2.4: Schematic of two faces with a common edge and their respective normal. Courtesy of [41]

The polyhedron shape approach is based on the concept that any body of arbitrary shape can be approximated with a polyhedron having a variable number of triangular faces (see Figure 2.5). Exploiting the analytic form of the gravitational potential of a homogeneous polyhedron with such faces, it is possible to evaluate the field generated by any irregularly-shaped body by collecting all elementary contributions together.

The closed-form analytical expression of the exterior gravitational influence of a constant-

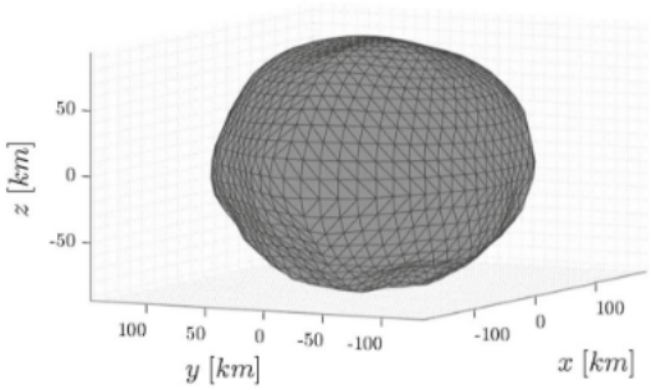

Fig. 2.5: Asteroid Psyche polyhedral model. Courtesy of [42]

density polyhedron guarantees that the gravity field is exact in any portion of space for the given shape and density. Notwithstanding all these positive features, this method is markedly expensive in terms of the computational cost, as the entire surface must be summed over to achieve one single force value, and certainly this cost increases with the resolution of the shape discretization. [43]
After some mathematical manipulations of the potential U, well described in [40], one arrives to the following expressions that model the polyhedron gravitation.

$$U = \frac{1}{2}G\sigma \sum_{e\in \text{ edges}} \mathbf{r}_e \cdot \mathbf{E}_e \bullet \mathbf{r}_e \cdot L_e - \frac{1}{2}G\sigma \sum_{f\in \text{ faces}} \mathbf{r}_f \cdot \mathbf{F}_f \bullet \mathbf{r}_f \cdot \omega_f \tag{2.1.8}$$

$$\nabla U = -G\sigma \sum_{e\in \text{ edges}} \mathbf{E}_e \bullet \mathbf{r}_e \cdot L_e + G\sigma \sum_{f\in \text{ faces}} \mathbf{F}_f \bullet \mathbf{r}_f \cdot \omega_f \tag{2.1.9}$$

$$\nabla\nabla U = G\sigma \sum_{e\in \text{ edges}} \mathbf{E}_e \cdot L_e - G\sigma \sum_{f\in \text{ faces}} \mathbf{F}_f \cdot \omega_f \tag{2.1.10}$$

$$\nabla^2 U = -G\sigma \sum_{f\in \text{ faces}} \omega_f \tag{2.1.11}$$

Symbols G and σ represent the gravitational constant and the polyhedron's constant density. Suffixes e and f indicate edge and face, respectively. Each polyhedron face has an outward-pointing face normal vector $\hat{\mathbf{n}}_f$ and face dyad $\mathbf{F}_f = \hat{\mathbf{n}}_f \hat{\mathbf{n}}_f$. Each edge of each face has an outward-pointing edge normal vector fife perpendicular to both $\hat{\mathbf{n}}_f$ and the edge. For the edge connecting vertices 1 and 2 shared by faces A and B, the edge dyad is $\mathbf{E}_{12} = \hat{\mathbf{n}}_A \hat{\mathbf{n}}_{12}^A + \hat{\mathbf{n}}_B \hat{\mathbf{n}}_{21}^B$, with other $\mathbf{E}_s$ defined similarly. $\mathbf{r}_i$ represents the vector from the variable field-point location to polyhedron vertex Pi, and let $r_i = \|\mathbf{r}_i\|$ be its length. For the polyhedron edge connecting vertices P_i and P_j of constant length e_{ij}, the dimensionless

per-edge factor L_e is:

$$L_e \equiv \int_e \frac{1}{r}\,\mathrm{d}s = \int_{P_i}^{P_j} \frac{1}{r}\,\mathrm{d}s = \ln \frac{r_i + r_j + e_{ij}}{r_i + r_j - e_{ij}} \tag{2.1.12}$$

For a triangular face f bounded by vertices P_i,P_j,P_k the dimensionless per-face factor ω_f is expressed by:

$$\omega_f = \iint_{\text{triangle}} \frac{\Delta z}{r^3}\,\mathrm{d}S = 2\arctan \frac{\mathbf{r}_i \bullet \mathbf{r}_j \times \mathbf{r}_k}{r_i r_j r_k + r_i\,(\mathbf{r}_j \bullet \mathbf{r}_k) + r_j\,(\mathbf{r}_k \bullet \mathbf{r}_i) + r_k\,(\mathbf{r}_i \bullet \mathbf{r}_j)} \tag{2.1.13}$$

Using these definitions, the gravitational potential, attraction, gravity gradient matrix, and Laplacian of a constant density polyhedron are expressed intrinsically, in closed form as above.

2.1.4. Mascon Model

The mascons approach is surprisingly simple from a conceptual point of view because it uses several point masses to reproduce the body's mass distribution. The resulting gravity field depends on the number of employed masses, and on how they are distributed. While, the mass of the total body is always preserved, there exist different methods to distribute the point masses in the body's domain. Classical strategies employ an evenly spaced grid and are referred to as *gridded mascons approaches.*
The gravitational potential of the whole body, making use of N_m mascons, is:

$$U = G \sum_{i=1}^{N_m} \frac{m_i}{r_i} \tag{2.1.14}$$

where m_i and r_i are, respectively, the mass value and the distance from each point mass. The previous equation converges to the true gravitational field for $N_m \to \infty$.
In [43] the point masses are also distributed according to an optimization process and the obtained results are presented and then compared with those related to the polyhedron approach and mascon gridded version.

From the comparison, it emerged that the polyhedron approach, especially if the representation of the body is particularly accurate, produces superlative results, but it is computationally expensive. The fidelity of the field is only limited by the accuracy of the shape representation; moreover, the Laplacian of the potential is immediately available to determine if a field point is outside or inside the body. The required time to evaluate the field is linearly increasing with the number of polyhedron's faces, while the errors of the model decrease with the square root of the same quantity. Having this information, an

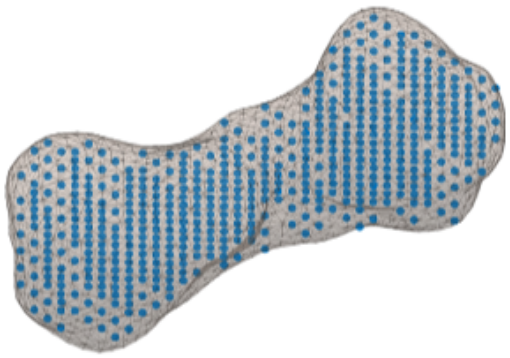

Fig. 2.6: Gridded mascons model applied to 216 Kleopatra. Courtesy of [43]

acceptable level of accuracy and computational effort can be established according to the current needs.
The mascons approach is markedly faster and produces good results if the field point is far enough from the surface of the body. In general, it produces poor results if it is applied to elongated bodies. The optimized version of this technique improves the performances of the standard version up to its theoretical limit: the error decreases by one order of magnitude for an increase of three orders of magnitude in the number of mascons. However, over a certain number of point masses, the optimization process is not effective anymore and the gridded mascons approach is sufficient to have an acceptable result.
The conclusion of [43] is that the most efficient and effective gravity model is a combination of both approaches. The resulting optimum Lo-Fi technique uses a polyhedron with a moderate number of faces to compute the field close to the surface of the body, and the optimized mascons with a reasonable number of masses when the distance from the centre of mass is large enough. The switch between the two models happens at a distance where the gap between the two techniques is extremely limited, in a way to maintain the continuity of the field.

2.2. Augmented Hill Problem

Firstly introduced by George Hill to study the motion in the vicinity of the Moon in 1878, the Hill Problem [44] represents a particular case of the Circular Restricted Three-Boby Problem (CR3BP). [45] It describes the scenario where the motion is in the neighborhood of the secondary body and the mass of the latter is much smaller than the one of the primary. The classical formulation, although employed in previous works and widely explored [46, 47], does not account for one of the major perturbations involved in the considered system: the Solar Radiation Pressure (SRP). [3] The evolution of the Hill problem, taking in account a radiating primary, is also known as Photogravitational Hill Problem or Augmented Hill Problem (AHP). [48]
Assuming an asteroid rotating around the Sun with period T_a, it can be considered the

rotating reference system - namely the Hill frame - centered in the center of mass of the asteroid (or the barycenter of the binary in our case), given by $\hat{\mathbf{x}}_{Hill}$ (anti-solar direction), $\hat{\mathbf{z}}_{Hill}$ (asteroid angular momentum) and $\hat{\mathbf{y}}_{Hill}$ to complete the orthogonal frame. In this case the Equations of Motion (Equation 2.2) normalized using as unit of length $[l] = (\mu/\omega^2)^{1/3}$ and unit of time $[t] = 1/\omega$, where μ is the asteroid gravitational parameter and $\omega = 2\pi/T_a$ read [46]:

$$\ddot{x} - 2\dot{y} = -\frac{x}{r^3} + 3x + \beta \tag{2.2.1}$$

$$\ddot{y} + 2\dot{x} = -\frac{y}{r^3} \tag{2.2.2}$$

$$\ddot{z} \quad = -\frac{z}{r^3} - z \tag{2.2.3}$$

where $r = \sqrt{x^2 + y^2 + z^2}$ and β is the non-dimensional SRP acceleration. The approximation to the vicinity of the asteroid, or secondary body, means we include the Sun's third-body effect in the dynamics instead of the absolute gravitational attraction felt by the particle from the Sun [46].

The SRP is assumed to be constant and acting along the Sun-asteroid direction. The non-dimensional SRP acceleration, β, is then obtained by normalizing the traditional SRP acceleration, a_{SRP}, for a cannonball model [49], i.e., with a constant exposed area and attitude, which yields Equation 2.2.4:

$$\beta = \frac{a_{SRP}}{[l]/[t]^2} = \frac{(1 + C_R)\, P_0}{m/A \mu^{1/3} \mu_S^{2/3}} \tag{2.2.4}$$

where C_R is the reflectivity coefficient or albedo, $P_0 \approx 1.02 \times 10^{17}$ kg m s^{-2} is the solar constant, m/A is the mass-to-area ratio, and μ_S is the gravitational parameter of the Sun. Still following [46], the system of Equation 2.2 admits an energy integral (Equation 2.2.5) known as the Jacobi constant C:

$$\begin{cases} C = 2\tilde{U} - V^2 = 3x^2 + 2\beta x + \dfrac{2}{r} - z^2 - \left(\dot{x}^2 + \dot{y}^2 + \dot{z}^2\right) \\ \tilde{U} = \dfrac{3}{2}x^2 + \beta x + \dfrac{1}{r} - \dfrac{z^2}{2} \\ V = \sqrt{(\dot{x}^2 + \dot{y}^2 + \dot{z}^2)} \end{cases} \tag{2.2.5}$$

where $\tilde{U}$ and V represent, respectively, the effective potential and kinetic energies of the system. Since V cannot be negative, it follows that

$$V^2 = 2\tilde{U} - C \geq 0$$

which translates into the region of accessible motion of a particle (condition $2\tilde{U} \geq V$). The boundaries of these regions are called Zero Velocity Curves (ZVC) and can give important insights on the motion of particles in Three-Body environment. [50]
Unlike the five equilibrium conditions (Lagrangian points) associated with the CR3BP, it is easy to derive - setting the left-hand side of Equation 2.2 to zero - that the classical Hill Problem ($\beta = 0$) admits two equilibrium points, located at:

$$x = \pm \left(\frac{1}{3}\right)^{1/3}$$

While for β values different from zero, the the Lagrangian points are found by choosing the real roots of the polynomials:

$$3x^3 + \beta x^2 \pm 1 = 0$$

AHP has been widely characterized in terms of equilibrium points and exploiting their orbit families both for low [48] and high [51] values of SRP.
In this work the AHP is employed to perform analyses about the displacement along preferred orbits of the ejecta after a certain period following the impact of DART with Didymoon. The characteristics of the AHP model used in this work are specialized in chapter 3 to avoid repetitions.

2.2.1. Capture condition in the AHP

The focus of this work is to evaluate the possibility that ejecta particles remain bounded to the Didymos system. A method to assess the capture condition of an object to the source of gravity field in the contest of the AHP, based on the evaluation of the Jacobi constant in L_2 has been described by Scheeres [46] and is reported here.
When considering the case in which the SRP direction rotates with the orbiting body and the gravity source orbits the sun with a certain eccentricity, the equations of motion should be modified accordingly, leading to formulas dependent on the eccentricity and true anomaly of the asteroid. Such equations of motion admit a Jacobi integral which is not, in general, a constant of integration - unless the asteroid is in a circular orbit around the Sun ($e_s = 0$) - that reads [52]:

$$\Gamma = 2\,U(\mathbf{r}) - (1 + e_s cos\, f)[v^2 + z^2] \tag{2.2.6}$$

And whose differential with respect to the true anomaly can be expressed as follows:

$$\dot{\Gamma} = e_s sin\, f[v^2 + z^2] \tag{2.2.7}$$

Therefore the quantity is only conserved for a circular orbit or for an equilibrium point in the orbital plane. Therefore, considering the planar Zero Velocity Curves (z = 0), the relationship becomes invariant with respect to the true anomaly and reads:

$$\Gamma = 2\,U(x, y, z = 0) \tag{2.2.8}$$

To find the capture condition one should consider that the value of the Jacobi constant at the equilibrium points (namely Γ^*) is constant, and in particular can be found approximately as:

$$\Gamma^*_{\pm} \approx 3^{4/3} \pm 2\left(\frac{1}{3}\right)^{1/3} \beta - \frac{1}{9}\beta^2 + ... \qquad \beta \ll 1 \tag{2.2.9}$$

$$\Gamma^*_{+} \approx 4\sqrt{\beta} \qquad \beta \gg 1 \quad \& \quad x^* > 0 \tag{2.2.10}$$

$$\Gamma^*_{-} \approx -\frac{1}{3}\beta^2 \qquad \beta \gg 1 \quad \& \quad x^* < 0 \tag{2.2.11}$$

Combining the previous results shows that there is a simple sufficient criterion for the capture of an object at a body: if the value of Γ for an object is always greater than Γ^*_+, and the object is inside of the zero-velocity surface, then the spacecraft is definitely bound to the body.
Since the value of Γ changes over time, the satisfaction of the criterion at one time does not guarantee that it will be satisfied at some point in the future, so its use is somewhat limited. This does fit well, however, with using the criterion for shorter time spans over which this criterion provides useful results.

2.3. Cratering processes and ejecta fate modelling

Modelling the dynamics of particles about a minor body following an impact event is a challenging task due to the strongly perturbed environment, mainly by the SRP. Many studies have been carried on to assess the fate of ejecta around small bodies from an astrodynamics point of view around cometary nuclei [53], comets and asteroids with application to the mission Deep Impact to *comet 9P/Tempel* [54] and asteroids (e.g. *4769 Castalia* [55], *162173 Ryugu* [56, 57]).
The work from Scheeres [3] presents a comprehensive review about perturbations and models to study the evolution of the ejecta in reduced gravity frameworks. In the same work, a distinction per classes of the ejecta fate is reported (see Figure 2.7). In particular the classes can be described as follows:

- Class I: immediate reimpact, prior to periapsis passage
- Class II: Ejecta does not reimpact at the first periapsis passage, but eventually

reimpacts in the future

- Class III: Stable motion, ejecta is placed into a long-term stable orbit about the asteroid
- Class IV: Eventual escape, ejecta has at least one periapsis passage by the asteroid before it escapes
- Class V: Immediate escape, ejecta escapes from the asteroid prior to its first periapsis passage

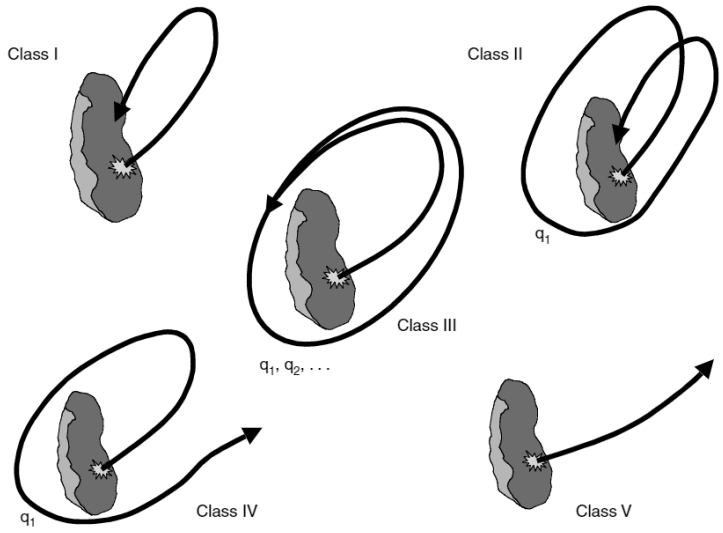

Fig. 2.7: The five classes of ejecta fate as defined in [3]

For the mission of interest for this work, specific studies have been performed up to date, both regarding the orbital stability assessment and the fate of the ejecta. For instance, Capannolo et al. [58] investigated families of bounded orbits in the close proximity of *Didymos* using a novel continuation technique. Ferrari et al. [34] described the methodology and design approach to find trajectories in the dayside of Didymos system to identify optimal orbits for the Milani CubeSat.
Yu et al. [59, 60] simulated the full scale ejecta fate as a consequence of the DART impact on Dimorphos, recording the history of the ejecta accretion and escape. The violent period of the ejecta evolution was found to be short, and many of the smaller particles were found to be swept out from the system due to SRP. However, large debris disposed on polar orbits were found to be more persistent with respect to low-latitude orbits. Ferrari et al. [6] studied the dynamics of ejecta fragments using GRAINS, a N-body Discrete Element Method (DEM) code, accounting for the translational and rotational dynamics of each ejecta fragment (non-spherical rigid-body) plus the interactions between them and with the environment. As a result, they found that higher density structures are more likely to be formed within the ejecta cone with consequences on the long-term fate. Rossi

et al. [61] performed moreover a sensitivity analysis with respect to the system parameters for the dynamics of the ejecta.
Aside from the dynamical environment considered, an important role in the assessment of particles' fate is played by the crater and impact modelling. In 1977 Donald E. Maxwell was one of the first researchers trying to offer analytical insights of the cratering processing the context of the combined studies of impact and explosion cratering physics. [62] He developed a simple model to describe the flow field of the target material, in order to predict the evolution of the crater and the ejecta. This model has become known in the literature under the name of *Maxwell Z-model*.
Indeed, the most widely employed semi-empirical laws to extrapolate the results of impact experiments at laboratory-scale to predict the outcome of planetary-scale event are the crater and ejecta scaling relationships, especially the version developed by Holsapple and Schmidt in 1987 [63], perfectioned in Housen and Holsapple [4]. Such relations, usually referred to as *Scaling Laws* are described in this work in subsection 2.3.1.
In 2006 Wünnemann et al. [64] developed the iSALE shock physics code, a multi-material, multi-rheology extension of the SALE (Simplified Arbitrary Lagrangian Eulerian) hydrocode [65] that was specifically designed for simulating impact processes. A 3D version of the code was also developed in 2011. [66] Both versions have been used in a variety of studies about space impacts [67], including some related to the DART mission [68, 69].
In 2021, Raducan et al. [68] investigated the effects of alternative projectile geometries on the DART impact outcome using iSALE shock physics code in two and three-dimensions to model vertical impacts of projectiles with a mass and speed equivalent to the nominal DART impact, into porous basalt targets. The outcome was that the simple projectile geometries investigated have minimal effects on the crater morphology.
In a work published at the beginning of 2022, Raducan et al. [69] set the basis for an extension of the scaling laws to oblique impacts.

2.3.1. Scaling Laws

Many studies have been performed regarding the so-called Scaling Laws. The outcomes of this semi-empirical models are correlations between the impactor and target properties and the transient crater relevant quantities, such as volume, radius, distribution of ejecta mass and velocity related to the radial distance from the impact point.
In this section is presented the formulation from [4], to be employed in this work. This model is intended for basic hypervelocity impacts on airless bodies, for which the impact is normal and the target material is a flat and homogeneous half infinite space. Moreover, the relations are derived by approximating the impact as a point source.
The relevant quantities that determine the outcome of a cratering events are divided into those related to the impactor and those related to the target. The impactor is assumed to be spherical with radius a, velocity U and density δ. The target is instead defined by its density ρ and a measure of the strength Y. If necessary, the viscosity of the target material

η, can be added, but for most planetary soils it can be easily discarded [70]. Moreover the body force field that affects the environment has to be considered and, being the most typical case the target gravitational field, it will be considered as a constant magnitude scalar g, directed downward. Figure 2.8 shows the schematics of the impact problem.

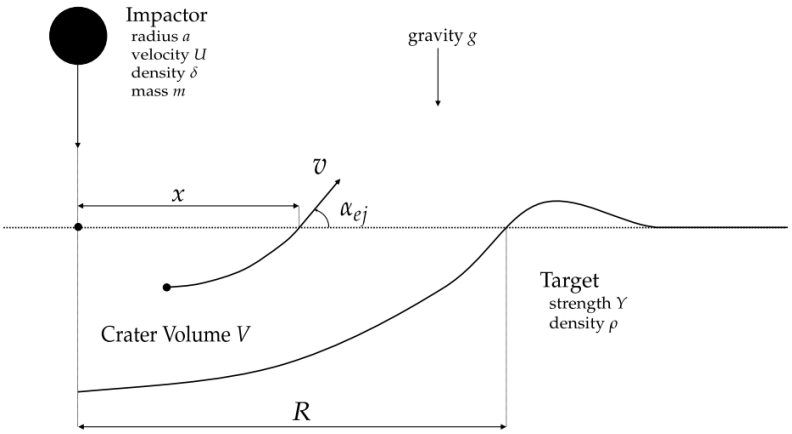

Fig. 2.8: Schematic of the impact problem as analyzed in [4]

The formulation of the final transient crater can thus be considered as follows:

$$V = f(a, U, \delta, \rho, Y, g) \tag{2.3.1}$$

By looking at the correlation one finds that 7 quantities containing 3 dimensions are involved. The 3 dimensions are length [L], mass [M] and time [T]. Consequently applying the Buckingham π Theorem, the free parameters in 2.10 are reduced to 4 adimensional groups.

$$\frac{\rho V}{4/3\pi a^3} = f\left(\frac{ga}{U^2}, \frac{Y}{\rho U^2}, \frac{\rho}{\delta}\right) \tag{2.3.2}$$

$$\pi_V = f\left(\pi_2, \pi_3, \pi_4\right) \tag{2.3.3}$$

Each group has a precise meaning. Specifically:

- $\pi_V = \rho V / \left(4/3\pi a^3\right)$ (also known as π_1) is the so-called Cratering Efficiency, i.e. the ratio between the mass occupying the crater before the impact and the mass of the projectile
- $\pi_2 = ga/U^2$ is the inverse of the Froude Number, representing the ratio among lithostatic pressure at a depth equal to one impactor radius and the induced dynamic pressure on the target.

- $\pi_3 = Y/\rho U^2$ determines the balance between the crustal material strength and the same dynamic pressure
- $\pi_4 = \rho/\delta$ relates the impactor and target densities. This very last group is typically dropped out of the function, since it is material dependent and can be easily defined by experiments and included in proportional constants, leading to Equation 2.3.4.

$$\pi_V = f\left(\frac{ga}{U^2}, \frac{Y}{\rho U^2}\right) \tag{2.3.4}$$

At this point it is straightforward to look at and compare the two terms related to π_2 and π_3, i.e. lithostatic pressure ρga and material strength Y. The preponderance of one term upon the other defines two distinct regimes of cratering.

- If $\rho ga \gg Y$ the gravity regime or gravity-dominated cratering is considered;
- If $Y \gg \rho ga$ the strength regime or strength-dominated cratering is considered.

In either case, the group related to the lower parameter can be discarded, leading to:

$$\begin{cases} \pi_V = f\left(ga/U^2\right), & \text{for gravity regime} \\ \pi_V = f\left(Y/\rho U^2\right), & \text{for strength regime} \end{cases}$$

In the real impact problem, the source of the perturbation is a finite dimensional body, the impactor. The actual properties of the impactor (a, δ and U) affect the solution only locally in the neighbourhood of the impact point and only at the beginning of the phenomenon. So for a radial distance from the impact point $x > a$ and for a time $t \gg a/U$ the source of the perturbation can be assumed to be zero-dimensional and the time of energy deposition infinitesimal. The simplification leads to a point source problem. [63] A point source problem is the limit of a problem where the initial time and size scales go to zero, while the extent of the perturbation goes to infinity by however keeping a certain parameter constant. This parameter, for the impact problem, is called Coupling Parameter and its definition is given by:

$$C = aU^{\mu}\delta^{v}$$

And the point source approximation is explicated in the following limit.

$$\lim_{a \to 0} aU^{\mu}\delta^{v} = C$$

The density scaling exponent ν is often assumed to be independent of material properties, with a value of about 0.4. On the other hand, the velocity scaling exponent μ depends on the target material properties and takes values between the theoretical limits of 1/3 if the

coupling parameter scales with the momentum of the impactor, and 2/3 if the coupling parameter scales with the impact energy.
Starting from these considerations, one can derive the following quantities :

- Crater volume
- Crater radius
- Ejecta velocity
- Ejecta mass and formation time

As this is a quite detailed topic, hereby are reported only the expression used in this work, as derived in 2012 by Holsapple and Housen [71]. Details on the derivation of such quantities can be found in [72]. Equation 2.3.5 represents the scaled radius of the crater, where H_2 is a constant. Equation 2.3.6 and Equation 2.3.7 represents the distribution of the ejection mass M and ejection speed v as functions of the radial distance x from the crater center. Also in this case additional constants n_1 and n_2 are present. Finally, in Equation 2.3.8 is found the number of regolith grains, where N_r is the reference number of the measured grains, while d_l and d_u determine the lower and upper limits of the full size range, respectively. All the constants are reported in the proper section dedicated to the ejecta generation in the context of this work (section 3.3).

$$R\left(\frac{\rho}{m}\right)^{1/3} = H_2\left(\frac{\rho}{\delta}\right)^{(1-3v)/3}\left(\frac{Y}{\rho U^2}\right)^{-\mu/2} \tag{2.3.5}$$

$$M(<x) = m\frac{3k}{4\pi}\frac{\rho}{\delta}\left[\left(\frac{x}{a}\right)^3 - n_1^3\right], n_1 a \leq x \leq n_2 R \tag{2.3.6}$$

$$v = UC_1\left[\frac{x}{a}\left(\frac{\rho}{\delta}\right)^v\right]^{-\frac{1}{\mu}}\left(1-\frac{x}{n_2 R}\right)^p, n_1 a \leq x \leq n_2 R \tag{2.3.7}$$

$$N(>d) = N_r d^{-2.8}, \quad d_1 \leq d \leq d_u \tag{2.3.8}$$

3 | Dynamical Model

The motion around small bodies usually differs in a significant manner from Keplerian motion because of their irregular and small gravity field. This implies a strong influence of the perturbations (such as the SRP) on the trajectory. The case of binary system makes moreover even difficult to correctly simulate the environment, due to the presence of an additional gravity field. It is therefore mandatory to set up a reliable model of the ambient such to achieve a good level of fidelity and compliantly design the mission.
In the context of this work, the aim is to evaluate if the ejecta could be bounded to the system in the Augmented Hill Problem. With this purpose, in this chapter is presented the environment of the binary system Didymos focusing on the solution adopted for the gravity field simulation and the related reference systems (section 3.1). In section 3.2 is specialized the dynamical setting employed, introducing the equations of motion and the link with the Augmented Hill Problem and finally in section 3.3 is described the cratering process and the generation of the initial conditions for the ejecta.

3.1. A model of (65803) Didymos

(65803) Didymos is an Apollo asteroid discovered on April 11, 1996 by Spacewatch at Kitt Peak. Its binary nature was discovered with photometric and radar observations obtained shortly after its close approach to Earth (at a minimum distance of 0.048 AU) during the period November 20–24, 2003 [73].
A radar reconstruction of the system is depicted in Figure 3.1.

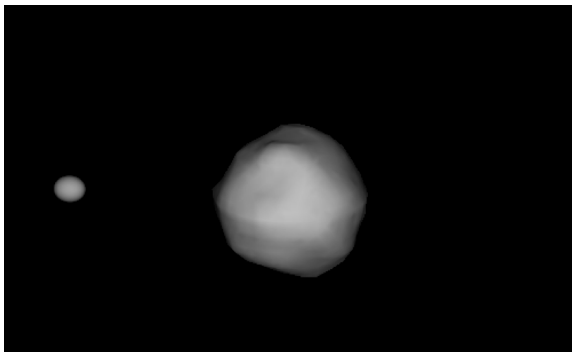

Fig. 3.1: Shape reconstruction of the Didymos system. Image of public domain, Naidu et al., AIDA Workshop 2016

The known parameters of Didymos are summarized in Tables 3.1 and 3.2. Note that the only dynamical parameters directly measured by the observations are the orbital period of the secondary around the primary, their orbital separation, the rotation period of the primary and the size ratio of secondary to primary. All other quantities (e.g. system's mass etc) are derived from these measured parameters. Detailed explanation can be found in [74], from which the majority of the data are taken if not explicitly specified otherwise.

Binary Orbit Solution of Didymos	
Nominal Orbital Pole	$\lambda = 270°$, $\beta = -87°$ [75]
Diameter ratio D_S/D_P	0.21 ± 0.01
Secondary orbital period P_{orb}	11.920 h +0.004 - 0.006 h
Secondary orbital eccentricity	< 0.03
Secondary orbital inclination	0°

Table 3.1: The binary orbit solution of Didymos

Several studies have addressed the binary relative dynamics between the primary (Didymos) and the secondary (Dimorphos) in recent years. [77, 78] This work is instead focused on modeling the motion of dust and therefore the motion of the two bodies is prescribed and not solved analytically. In particular, the data furnished by the up-to-date kernels for the HERA mission study have been employed. [79] The ephemeris of Didymos with respect to the solar system barycenter were available for the impact time, while for the position of Dimorphos have been used the ephemeris times available from kernels making sure to reproduce the correct initial condition for the propagation (see chapter 4).
Moreover, the following assumptions have been made based on the current knowledge of the binary system:

- the spin vector of Didymos is aligned to the angular momentum of Dimorphos around the primary
- the secondary is tidally-locked to the primary: its spin period is syncronized with his revolution period around Didymos
- the two bodies have the same equatorial plane, and their pole has ecliptic coordinates $\lambda = 270$ and $\beta = -87$ degrees, as retrieved from up-to-date Hera mission kernels [79]. The binary motion is therefore retrograde with respect to its barycenter.

The problem under study involves two shapes with well inferred or known characteristics, as summarized in Table 3.1. For what concerns the primary of the Didymos system, a polyhedral model is available from radar measurement and is presented in [80]. Moreover, the secondary, as per radar observations, could be assimilated to a triaxial ellipsoid. Therefore, given the above mentioned analyses and considering the scope of this work, the gravity of Didymos has been modeled by means of a constant density polyhedron and the force field created by Dimorphos through a triaxial ellipsoid model with semiaxes α, β, γ equal to 103, 77 and 66 m respectively. A model of the two bodies are reported in figure

Didymos dynamical and physical properties	
Heliocentric semi-major axis	$(1.6444327821 \pm 9.8 \times 10^{-9})$ AU
Heliocentric eccentricity	$0.383752501 \pm 7.7 \times 10^{-9}$
Heliocentric inclination (ecliptic)	$(3.4076499 \pm 2.4 \times 10^{-6})$ deg
Primary rotation period	(2.2600 ± 0.0001) h
Distance between component COMs	(1.18 +0.04/-0.02) km
Mean diameter of the primary D_P	0.780 km ± 10%
Mean diameter of the secondary D_S	(0.163 ± 0.018) km
Secondary (shape) elongation a_S/b_S	1.3 ± 0.2
and b_S/c_S (assumed)	>1 (assumed: 1.2)
Bulk density of P and S	$2170\,\mathrm{kg\,m^{-3}}$ ± 350%
Total system mass	$5.55 \pm 0.42 \times 10^{11}$ kg
Mean absolute magnitude (whole system)	18.16 ± 0.04
Geometric albedo (H)	0.15 ± 0.04

Table 3.2: Known dynamical and physical properties of the binary asteroid Didymos [76]

Figure 3.2. The validation of the gravity field generated by each of the models is reported in Appendix A.

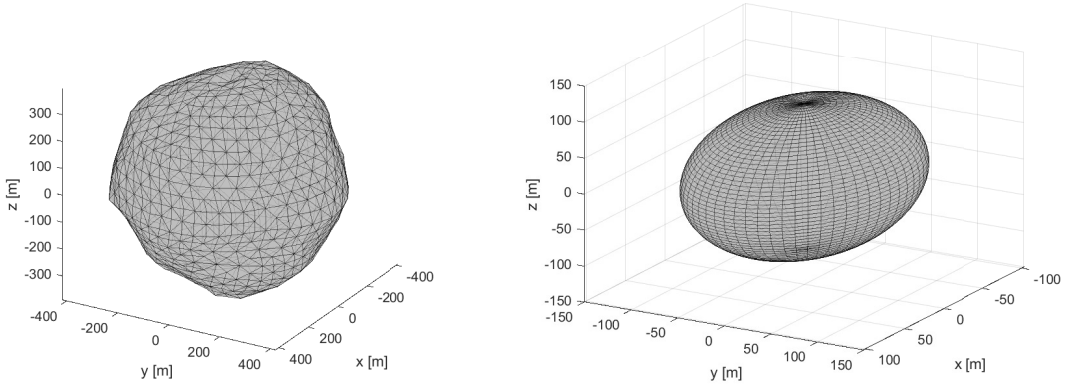

(a) Polyhedral shape of Didymos as derived from radar observations

(b) Triaxial ellipsoid model of Dimorphos. Semiaxes of 103, 77 and 69 meters.

Fig. 3.2: Didymos system primary (left) and secondary (right) shapes

3.1.1. Reference Frames

For what concerns the reference frames employed for describing the motion, in this work it has been adopted the same setup from Ferrari et al. [81]. With a major difference related to the presence of an additional reference system, namely *Hill reference frame*, whose characteristics have already been defined in section 2.2 and are reported again below. The reference systems are summarized as follows:

- A quasi-inertial reference frame centered in the baricenter of the Didymos system, namely D-ECLIPJ2000, whose axes are inertially fixed and parallel to the ECLIPJ2000 reference frame

- A body-fixed reference frame for Didymos, computed by retrieving data from the related ESA kernel
- A body-fixed reference frame for Dimorphos, whose x-axis points toward the system barycenter, z-axis has the same direction of the binary system pole and y-axis is defined accordingly
- A Hill frame, centered in the barycenter of the binary, given by $\hat{\mathbf{x}}_{Hill}$ (anti-solar direction), $\hat{\mathbf{z}}_{Hill}$ (asteroid heliocentric angular momentum) and $\hat{\mathbf{y}}_{Hill}$ to complete the orthogonal frame.

A schematic of all the reference systems is reported in Figure 3.3.

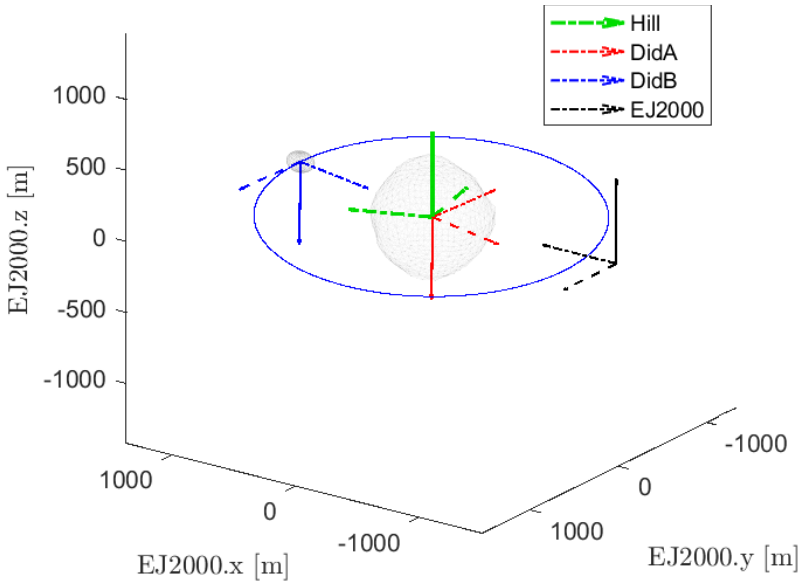

Fig. 3.3: Reference frames adopted and orbital plane of Dimorphos. The x,y and z axis of each frame are respectively dotted, dashed and fully colored. Notice that the D-ECLIPJ2000 is shown out of the system for the sake of clarity, but should be considered as centered in the Didymos system barycenter

3.2. Dynamical setting

In this section are presented the "*inertial*" and "*Hill*" frameworks, respectively. The first is the system in which the propagation of the ejecta particles occur, while the latter will be used for practical considerations with respect to the energy level of the particles, leading to the results of this study.

The accelerations in the proximity of the binary as computed in [81] with the same setup

of this work, are reported in Figure 3.4. In the next subsections, the relevant forces acting on an ejecta particles are characterized for both contexts.

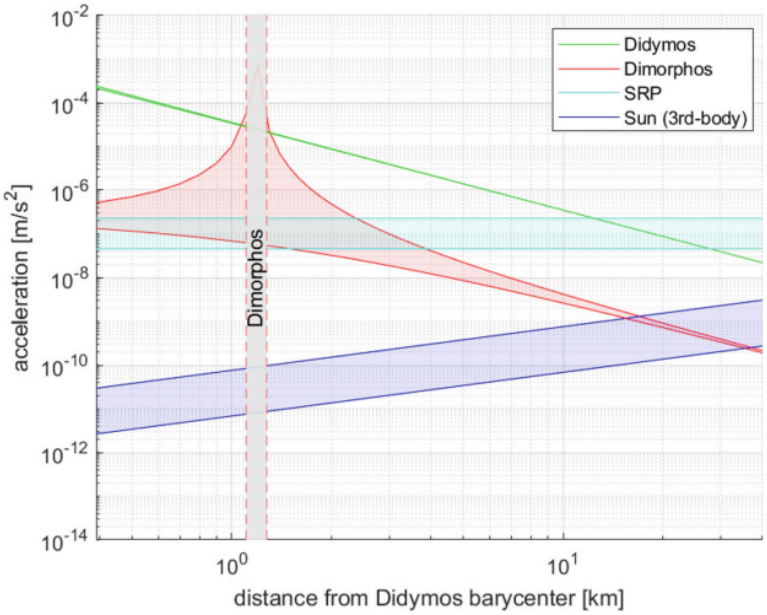

Fig. 3.4: Main accelerations in the proximity of Didymos binary system. Ranges between minimum and maximum values in the interval 01-Jan-2027 and 01-Jan-2028 are shown as shadowed region. Courtesy of [81].

3.2.1. Inertial framework

The motion of particles in the vicinity of the binary can be described through the general equation of motion (Equation 3.2.1):

$$\ddot{\boldsymbol{r}} = \boldsymbol{a}_{D_1} + \boldsymbol{a}_{D_2} + \boldsymbol{a}_{3b_S} + \boldsymbol{a}_{SRP} \tag{3.2.1}$$

In particular:

- $\boldsymbol{a}_{D_1}$ is the acceleration due to the gravity of Didymos
- $\boldsymbol{a}_{D_2}$ is the acceleration due to the gravity of Dimorphos
- $\boldsymbol{a}_{3b_S}$ is the acceleration due to the Sun, considered as a perturbing third body
- $\boldsymbol{a}_{SRP}$ is the acceleration due to the solar radiation pressure

The $\boldsymbol{a}_{D_1}$ has been computed through the gravitational potential of a constant density polyhedron [41] (Equation 3.2.2) as explained in section 2.1. Here the formulas are repeated in order to specify the transformation adopted between the reference frames.

$$\check{\boldsymbol{a}}_{D_1} = G\rho \left(\sum_{f \in \text{ faces}} \mathbf{F}_f \cdot \check{\boldsymbol{r}}_f \omega_f - \sum_{e \in \text{ edges}} \mathbf{E}_e \cdot \check{\boldsymbol{r}}_e L_e \right) \tag{3.2.2}$$

Terms of this equation are already specified in a previous chapter, however it is of interest highlighting that $\check{\boldsymbol{r}}_f$ and $\check{\boldsymbol{r}}_e$ are vectors from the field point to face f and edge e, respectively and are expressed in the asteroid body reference frame. The conversion from the body system to the D-ECLIPJ2000 is operated by mapping the rotation of the asteroid with respect to the inertial frame through a matrix R_1 and summing up the distance of the primary from the barycenter of the system, (namely d_1) as follows:

$$\boldsymbol{a}_{D_1} = \mathbf{R_1}\, \check{\boldsymbol{a}}_{D_1} \tag{3.2.3}$$

$$\boldsymbol{r}_f = \mathbf{R_1}\, \check{\boldsymbol{r}}_f + d_1 \tag{3.2.4}$$

$$\boldsymbol{r}_e = \mathbf{R_1}\, \check{\boldsymbol{r}}_e + d_1 \tag{3.2.5}$$

The same applies to Dimorphos, which has been modelled as a triaxial ellipsoid. As computation involves clearly the position of the point with respect to the body fixed reference frame, also here a rototranslation is required as follows:

$$\boldsymbol{a}_{D_2} = \mathbf{R_2}\, \check{\boldsymbol{a}}_{D_2} \tag{3.2.6}$$

$$\boldsymbol{r}_{ell} = \mathbf{R_2}\, \check{\boldsymbol{r}}_{ell} + d_2 \tag{3.2.7}$$

Where R_2 maps the rotation of the body reference frame with respect to D-ECLIPJ2000, r_{ell} is the vector to the point of the field and d_2 is the distance of the secondary from the barycenter of the system. Notice that the matrices $\mathbf{R_1}$ and $\mathbf{R_2}$ are time-varying.
The third-body effect of the Sun ($\boldsymbol{a}_{3b_S}$) is expressed in the Didymos barycenter, which in turn orbits the Sun. That is, a_{3b_S} models the Keplerian gravity gradient between the barycenter of Didymos system and the field point:

$$\boldsymbol{a}_{3b_S} = (\mu_S + \mu_D) \frac{\boldsymbol{r}_{D-S}}{\|\boldsymbol{r}_{D-S}\|^3} - \mu_S \frac{\boldsymbol{r}_{C-S}}{\|\boldsymbol{r}_{C-S}\|^3} \tag{3.2.8}$$

where $\mu_S = Gm_S$ and $\mu_D = G\left(m_{D_1} + m_{D_2}\right)$ are the gravitational constants of the Sun and Didymos system, respectively, $\boldsymbol{r}_{D-S}$ and $\boldsymbol{r}_{C-S}$ are the position vectors of Didymos system barycenter and the field point with respect to the Sun, in the D-ECLIPJ2000 reference frame.
The relative position between Didymos system barycenter and the Sun is retrieved at each epoch from the ephemerides data. Note that in our case $\mu_D << \mu_S$, and thus Equation 3.2.8 can be simplified to:

$$\boldsymbol{a}_{3b_S} \simeq \mu_S \left(\frac{\boldsymbol{r}_{D-S}}{\|\boldsymbol{r}_{D-S}\|^3} - \frac{\boldsymbol{r}_{C-S}}{\|\boldsymbol{r}_{C-S}\|^3} \right) \tag{3.2.9}$$

The last contribution of Equation 3.2.1 is due to Solar Radiation Pressure (SRP). This contribution is computed using a SRP cannonball model [82]:

$$a_{SRP} = \frac{P_0}{c} \left(\frac{D_{AU}}{\|\boldsymbol{r}_{C-S}\|} \right)^2 \frac{C_r A}{M} \hat{\boldsymbol{r}}_{C-S} \tag{3.2.10}$$

where P_0 $\left(1367 \text{ W/m}^2\right)$ is the solar flux at 1AU, c is the speed of light $\left(2.998 \times 10^8 \text{ m/s}\right), D_{AU}$ is the Sun-Earth distance $\left(1\text{AU} = 1.495 \times 10^{11}\text{m}\right), C_r$ is the reflectivity coefficient of the ejecta particle, A is its equivalent surface area, and M is its mass.
As seen, all the computation are done in the D-ECLIPJ2000 reference frame. Since the heliocentric inclination of Didymos is negligible (see Table 3.1), the particle trajectory as seen from the Hill reference frame,can be computed by means of a single rotation around the ecliptic north pole, being the x-axis of the Hill frame aligned with the sun-barycenter direction.

3.2.2. AHP formulation

Before introducing the formalism adopted for the AHP in the context of Didymos, some consideration shall be done.
Firstly, the forumlation of the Augmented Hill Problem for Didymos in this work represents an approximation of the real problem as it excludes the eccentricity of the heliocentric orbit, which in turn has an effect on the position of the equilibrium points when the true anomalies vary. [46] However, in this context the timescale analyzed is small if compared with the orbital period of the Didymos system, thus the variation in the position of the lagrangian points - more specifically of L_2, as L_1 loses its significance drifting away from the body towards the Sun - has been neglected, relying on a classical Hill problem. Nevertheless, as described in [46] and detailed in subsection 2.2.1, for the purpose of this thesis is not necessary to switch to an elliptical description of the AHP, as the condition for an object to be bound to the minor body can be expressed in the circular framework.
A second consideration is related to the potential employed in the AHP equations of motion. In fact, the shape-based gravitational field of the two bodies could be employed. However, here we only account for a point mass field, because up to a certain level of approximation, the field is practically coincident with the one generated from a single (equivalent) point mass. [81]
The adimensionalized equations of motion are reported here again as a reference:

$$\ddot{x} - 2\dot{y} = -\frac{x}{r^3} + 3x + \beta \tag{3.2.11}$$

$$\ddot{y} + 2\dot{x} = -\frac{y}{r^3} \tag{3.2.12}$$

$$\ddot{z} \quad = -\frac{z}{r^3} - z \tag{3.2.13}$$

where $r = \sqrt{x^2 + y^2 + z^2}$ and β is the non-dimensional SRP acceleration. The SRP is assumed to be constant and acting along the Sun-asteroid direction. The non-dimensional SRP acceleration, β, is then obtained by normalizing the traditional SRP acceleration, a_{SRP}, for a cannonball model [49], i.e., with a constant exposed area and attitude, which yields (Equation 3.2.14):

$$\beta = \frac{a_{SRP}}{[l]/[t]^2} = \frac{(1 + C_R)\, P_0}{m/A \mu^{1/3} \mu_S^{2/3}} \tag{3.2.14}$$

where C_R is the reflectivity coefficient or albedo, $P_0 \approx 1.02 \times 10^{17}$ kg m s^{-2} is the solar constant, m/A is the mass-to-area ratio, and μ_S is the gravitational parameter of the Sun. Considering a spherical particle of radius R, the mass-to-area ratio can be expressed as:

$$m/A = \frac{4/3 \rho \pi R^3}{4\pi R^2} = \frac{2}{3} \rho \pi R \tag{3.2.15}$$

The data used in the context of this problem are reported in table Table 3.3.

$M_p[kg]$	$M_s[kg]$	ρ $[kg/m^3]$	μ $[km^3/s^2]$	T_a [days]	C_R
5.229×10^{11}	4.8633×10^9	2170	3.5223×10^{-8}	770	0.50 [83]

Table 3.3: Didymos parameters for the Augmented Hill problem

As discussed in section 2.2 and verified in Appendix A, the Lagrangian points in the Hill problem shift from their initial position based on the intensity of the acting SRP. The shift in Lagrangian points for the Didymos system is shown in Figure 3.5. It can be noticed how, starting from equal and opposite values (about 110 km), the L_1 shifts to $-\infty$ as the adimensional SRP increases, losing of significance for our problem, which involves high values of solar pressure. On the contrary, the L_2 asymptotically approaches the body.

Moreover, the Zero Velocity curves of the problem are reported with respect to two different values of β (Figure 3.6) clearly showing how, as the adimensional SRP rises, the L_1 zone becomes unaccessible to the motion.

To make apparent the relation between β and other parameters, such as the size of the particle, (Table 3.4) summarizes the quantities of interest. It is worth to highlight that in this thesis the particles of interest will be in the range 0.1 to 100 millimeters in diameter,

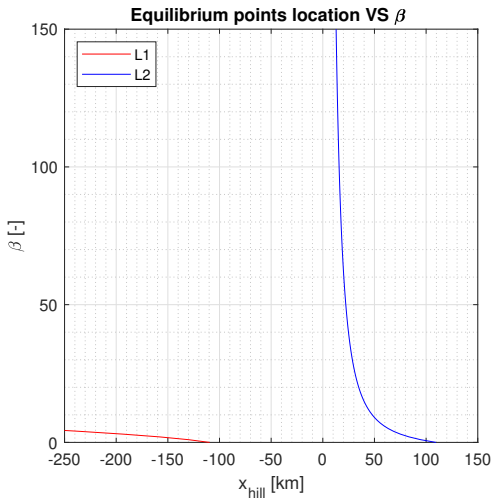

Fig. 3.5: Position on the x-axis of the equilibrium points in the AHP for Didymos with respect to the adimensional SRP

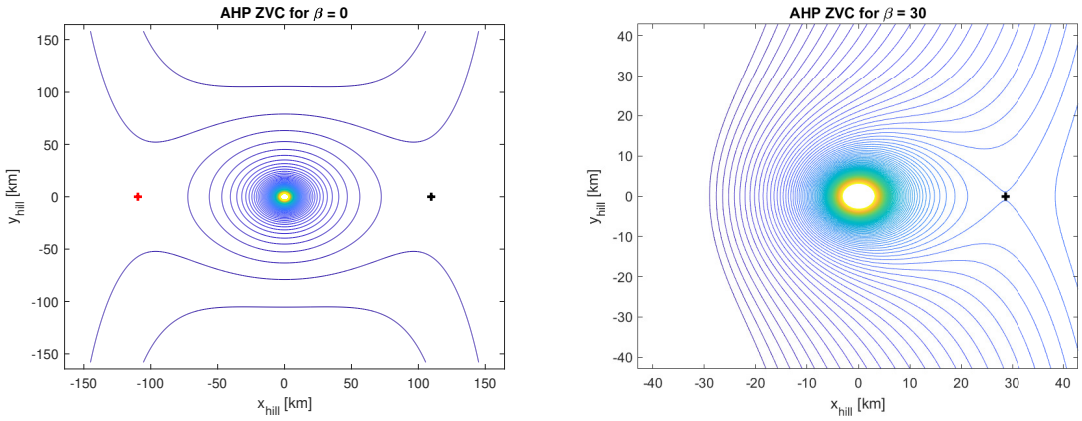

Fig. 3.6: Zero velocity curves variation for adimensional SRP equal to zero (left) and thirty (right)

which in turn corresponds to values of β starting approximately from 10 and beyond, as it can be observed from the table.

3.3. Ejecta modelling

As seen, the Scaling Laws depend upon the materials considered for both the asteroid and the projectile.

Here we assume that the material representative of Dimorphos is Sand/Fly Ash (SFA), a high porosity and low strength material, in accordance to Cheng et al. [84] that retain it may be a good analog for the surface of the secondary.

The assumed parameters for SFA are reported in Table 3.5 and are taken from Housen and Housapple [4]. The gravity acceleration of Dimorphos at the impact site has been

β	m/A	d [mm]	a_{SRP} $[m/s^2]$	C_{L_2} [-]	x_{L_2} [km]
0	-	-	0	4.3267	109.59
1	1794.1	789.4912	1.4099e-09	5.6133	94.551
5	358.81	157.8982	7.0493e-09	9.4799	63.456
10	179.41	78.9491	1.4099e-08	12.936	47.857
30	59.802	26.3163	4.2296e-08	22.008	28.6
50	35.881	15.7898	7.0493e-08	28.344	22.259
100	17.941	7.8949	1.4099e-07	40.03	15.782
150	11.96	5.2632	2.1148e-07	49.01	12.895
200	8.9703	3.9474	2.8197e-07	56.584	11.171
250	7.1762	3.1579	3.5246e-07	63.258	9.9929
300	5.9802	2.6316	4.2296e-07	69.292	9.123
500	3.5881	1.5789	7.0493e-07	89.449	7.0678

Table 3.4: Relationship between non-dimensional SRP acceleration (β), mass-to-area ratio (m/A), particle radius (R), dimensional SRP acceleration (a_{SRP}), Jacobi constant of the L2 point (C), and position of the L2 point.

computed through the straightforward formula $g_{dms} = \mu_{dms}/r_{imp}$ where the numerator is the gravity constant of Dimorphos and the distance of the impact site from the center of Dimorphos is $r_{imp} \approx 79$ m.

Y [MPa]	ρ $[kg/m^3]$	H2	μ	C1	k	p	ν	n1	n2	g_{dms} $[m/s^2]$
0.004	2170	0.4	0.46	0.55	0.3	0.3	0.4	1.2	1	5.2×10^{-5}

Table 3.5: Scaling parameters for the target

The projectile considered in this work to simulate the DART spacecraft, has the following properties: a mass M_p of 560 kg, an impact velocity $U = 6580$ m/s and an equivalent radius (namely a) of 0.686 m. From the mass and the radius one can retrieve the projectile bulk density (δ) using a simple inverse formula:

$$\delta = \frac{3M_p}{4\pi a^2} \tag{3.3.1}$$

The parameters for the impactor are summarized in Table 3.6.

a [m]	δ $[kg/m^3]$	U $[m/s]$	$M_p[kg]$
0.686 [85]	1070	6580 [86]	560 [86]

Table 3.6: Scaling parameters for the impactor

Having all the needed parameters, the regime to be used for computing the initial conditions based on the scaling laws reported in subsection 2.3.1 can be finally assessed. As the material strength Y reported in Pa is much higher than the product $\rho\, g_{dms}\, a$, it is apparent that the cratering process is dominated by the target strength.

3.3.1. Cratering process and particles size distribution

The outcome of a hypervelocity impact is strictly related to the material of the impacting means and the conditions of the impact itself, such as the direction of the impact, the temperature and many others.
Employing the scaling laws already described and here reported for the sake of clarity, the crater radius can be computed, along with the mass of the ejecta based on the particle size, the velocity distribution and the radial position of the particles in the crater. As seen, the dimensional crater radius in strength regime can be computed as:

$$R = H_2 \left(\frac{\rho}{\delta}\right)^{(1-3v)/3} \left(\frac{Y}{\rho U^2}\right)^{-\mu/2} \left(\frac{\rho}{M_p}\right)^{-1/3} \tag{3.3.2}$$

Which in the case of the DART impact and the data presented above, resulted to be 6.7949 meters.
Following [87], that studied the cumulative size-distribution of the granular material on the surface of Itokawa, a power law matches a wide range of particle sizes. The log-log slope is about -2.8 , which gives an estimate of the amount of cumulative number N of regolith grains, as expressed in the following equation:

$$N(>d) = N_r d^{-2.8} \tag{3.3.3}$$

$$N_r = \frac{9kM_p}{28\pi^2\delta\left(\sqrt[5]{d_{\max}} - \sqrt[5]{d_{\min}}\right)} \left[\left(\frac{n_2 R}{a}\right)^3 - n_1^3\right] \tag{3.3.4}$$

The number of particles within each size interval of interest $[d_{i-1}, d_i]$ is obtained from:

$$N_r \left(d_{i-1}^{-2.8} - d_i^{-2.8}\right), i = 1, 2, \ldots, w \tag{3.3.5}$$

In Table 3.7 is reported the number of particles for three diameter ranges, namely [0.1 - 1] mm, [1 - 10] mm and [10 - 100] mm.

Size range [mm]	Number of particles
10 - 100	4.2925e+12
1 - 10	6.8032e+09
0.1 - 1	1.0782e+07

Table 3.7: Number of particles within specified size ranges

As it can be noticed the number of generated particles is huge. In the analysis will be considered a subset of these ranges. More details on this topic will be given later on.
Completing the scaling laws, whose verification is reported in Appendix A, the distribution

of the ejection mass and speed as a function of the radial distance x are found according to Equations 3.3.6 and 3.3.7:

$$M(<x) = m\frac{3k}{4\pi}\frac{\rho}{\delta}\left[\left(\frac{x}{a}\right)^3 - n_1^3\right] \qquad n_1 a \leq x \leq n_2 R \tag{3.3.6}$$

$$v = UC_1\left[\frac{x}{a}\left(\frac{\rho}{\delta}\right)^v\right]^{-\frac{1}{\mu}}\left(1 - \frac{x}{n_2 R}\right)^p \qquad n_1 a \leq x \leq n_2 R \tag{3.3.7}$$

The above formulas define a unique continuous distribution of the scaled ejected material, and provide a mathematical description of the initial phase of the ejecta cloud. Therefore, a discretization should be applied to define the size of each particle.
Particularly, here has been adopted the following discretization to generate a set of particles that follows the PSD ensuring mass conservation. It is based on a random number generator and an inverse transformation of the distribution function as described in [60]. Having defined the ranges of interest as above, namely $[d_0 - d_1]$, N_s uniformly distributed points are created within the interval, where N_s is the number of sample particles.

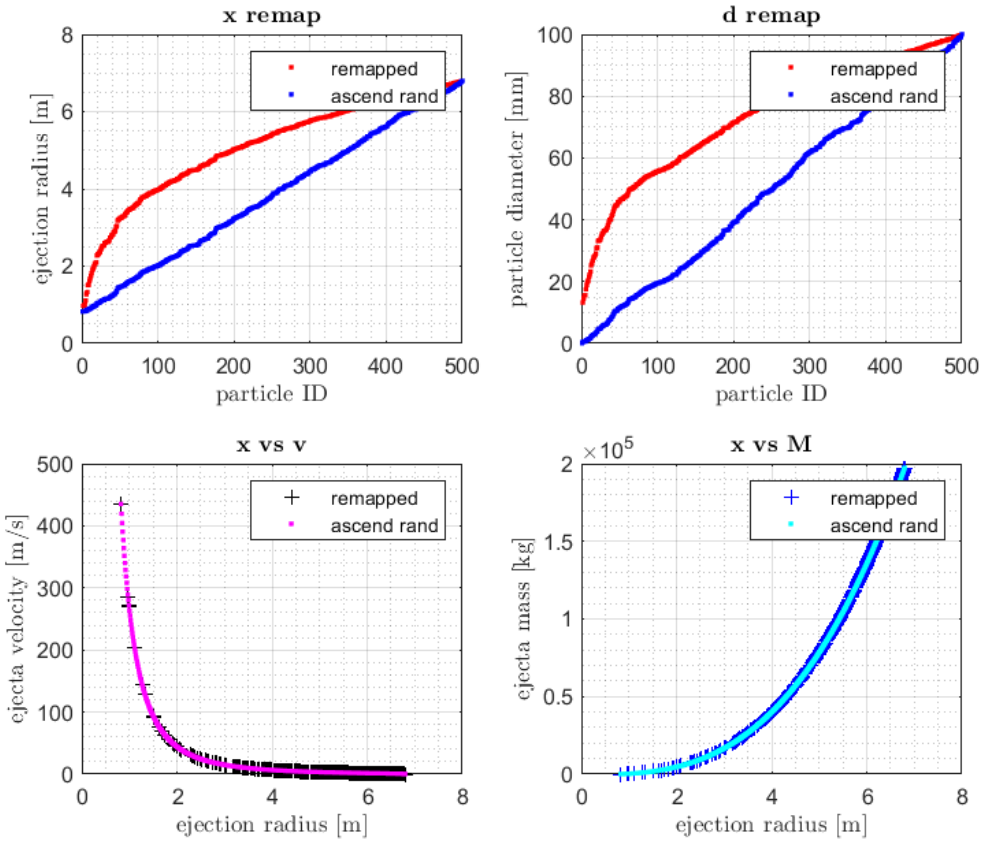

Fig. 3.7: Top: remapping of the ejecta radial position and diameter. Bottom: velocity and mass distribution with respect to the radial position randomly generated and then reordered in ascending values (dots) and remapped (crosses). All plots are over a 500 particle sample.

Then, the following transformation (Equation 3.3.8) is used to remap the sample diameters still following the power law. Notice that t is the exponent of the power law used to map the particles distribution, in this case equal to 2.8.

$$d' = \left[\frac{d - d_0}{d_1 - d_0} \left(d_1^t - d_0^t \right) + d_0^t \right]^{1/t} \tag{3.3.8}$$

The same applies to the distances from the center of the crater x, i.e. the departure points of the particles along the radius, as of Equation 3.3.9:

$$x' = \left[\frac{x - x_0}{x_1 - x_0} \left(x_1^3 - x_0^3 \right) + x_0^3 \right]^{1/3} \tag{3.3.9}$$

A visualization of the described parameters is reported in Figure 3.7 for a sample of 100 particles to show the trend. It is crucial to notice that initial and final values of the interval are remapped into themselves. Also, it can be observed how the highest velocity reached through the scaling laws is of 450 m/s, well beyond the escape velocity of the Didymos system.

3.3.2. Ejecta Initialization

As discussed earlier, a reduction in the sample is needed, mainly for two reasons. The first is related to the computational effort required to propagate the trajectories, and the second, more important, is related to the scope of this work. In fact, the objective is to study the fate of the ejecta that could possibly remain bounded to the binary system, i.e. particles whose velocities lie within a certain interval. Such interval can be found based on the analysis of [60] on the dependence of fate of the ejecta from the velocity distribution. The important values to be noted are:

- the escape velocity from Dimorphos' surface (assuming a single body) is 8.9 cm/s;
- the escape speed from the binary system at the Dimorphos distance (i.e. 1.18 km) is about 24.4 cm/s;
- the orbital speed of Dimorphos around the primary of about 17.3 cm/s;

This means that:

- the ejecta with $v \ll 8.9$ cm/s will be reaccreted by Dimorphos;
- the ejecta with $v \gg 60$ cm/s will tend to escape unless accreted on the primary
- those with moderate values will have the opportunity to be trapped into temporary orbits in the binary system and end up in various fates

Based on these consideration, the sample should be reduced such to fit the specified velocity

range $v_e \in [8.9, 24]$ cm/s. This in turn translates in the definition of a critical radius, i.e. after which the particles have the defined upper velocity or lower. In this case such radius have been found to be 6.7191 m, very close to the crater edge. In Figure 3.8 is reported the visualization of such limiting velocities.

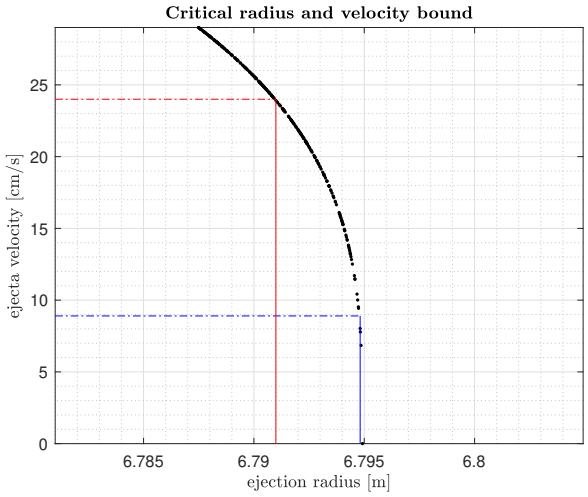

Fig. 3.8: Velocity bound of interest, the vertical red line represents the critical radius. Seeds set to 100000 for visualization purposes.

Once the sample has been reduced, it is needed to further manipulate the parameter given by the Scaling Laws to set the initial conditions for the propagation of the ejecta. Before proceeding, some considerations have to be made about the impact modeling and position on the surface of Dimorphos.
In this work, according to the scaling laws employed, the impact has been considered perpendicular to the local surface of the secondary. This implies a symmetry in the impact outcome.
As for the angular distribution of the launching directions, hereby it has been adopted a typical launching angle of 45° for all the sampled particles, which is a generic value according to the assumptions on the momentum transfer in asteroid impacts. [71]

Taking in account that DART will target the leading edge of the secondary (i.e. on the negative body y-axis of Dimorphos, as per our reference systems) to reduce its orbital period, the investigation is focused on an hypothetical crater in the motion direction. It has to be noticed that the current estimate of the impact point elevation is of 16.5 degrees. Thus, the crater positioning represents a further assumption, nevertheless adopted in other works.

To generate proper initial conditions according to our reduced set, we manipulate the results of the scaling laws as follows.

- generate 36 equispaced points (every 10 deg) over 10 circles of radius $x \in [6.7191, 6.7195]$ located on the surface of Dimorphos. For each circle, this is done such to cover the

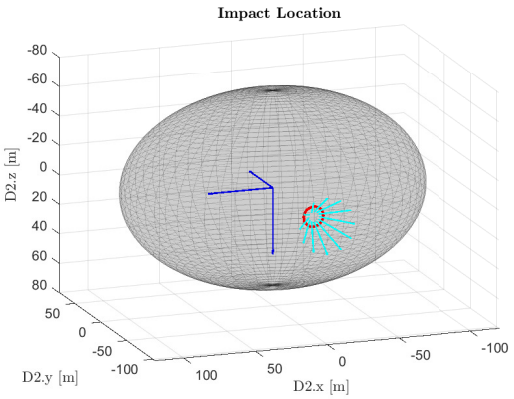

Fig. 3.9: Impact location (crater) considered in this work. Blue axes correspond to the body reference frame of Dimorphos

ejecta cone completely

- retrieve the associated velocity versor, inclined by 45° outward from the crater center
- scale the velocity unit vector by the corresponding magnitude, coming from the scaling laws velocity distribution
- perform the relevant transformations to retrieve the initial conditions for propagation in the D-ECLIPJ2000 reference frame

In Figure 3.9 is shown an example of particles distribution, where the points are equispaced of 30 deg for the sake of visualization. The origin of the vectors are the positions of the impact points along the crater. It is assumed a conical and equally spaced distribution of the particles in order to better characterize our results. As said, the particles have been assigned velocities according to the scaling laws (see Figure 3.8).

4 | Simulation and Results

As stated, the objective of this thesis is to evaluate the condition for which the orbits of the ejecta remain bounded to Didymos or are likely to escape. The simulation has been conducted through `MATLAB` and implemented in compliance with the theoretical framework expressed in the previous sections.
The initial time has been set to 4 October 2022 at 9:48:00, i.e. the DART impact time, adopting the configuration of the system as estimated by Cheng et al. [85], shown in Figure 4.1. It has to be noticed that no change in the orbit of Dimorphos is accounted for after the impact in this simulation.

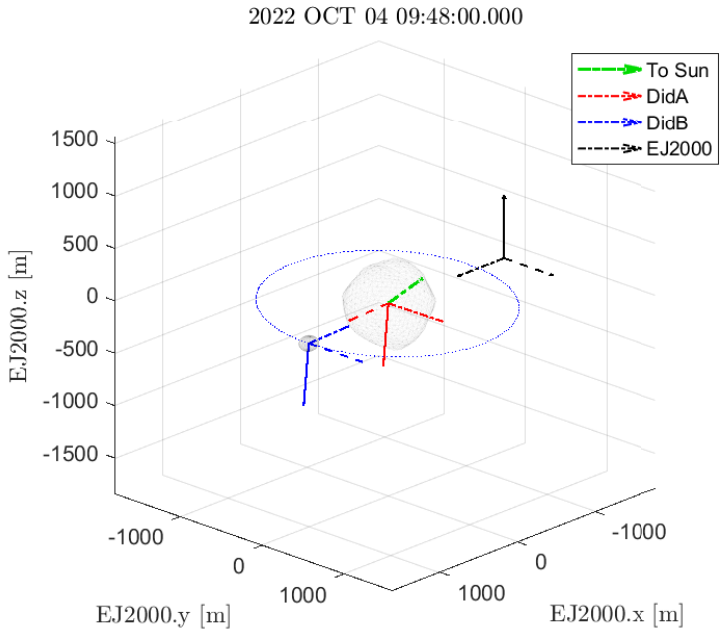

Fig. 4.1: Didymos system configuration at time 4 October 2022 09:48 UTC

INSERISCI PLOT ORBITA DIDYMOS

A set of particles have been initialized (see subsection 3.3.2) and propagated in the D-ECLIPJ2000 reference frame by means of a built-in `ode113` integrator. The propagation time has been set to 6 hours, according to Yu et al. [59], that simulated the behaviour of the ejecta cloud for 14 days concluding that orbiting particles are more likely to survive within the first six hours from the impact, while after that time the majority is swept out

from the system due to the SRP.
Three propagations have been made, assigning the same diameter to all the particles in each simulation, in order to characterize the patterns that may arise. With this setup the final simulation time was of about 4 hours.
As per the diameters, the three values reported in Table 4.1 have been chosen, based on the results of Table 3.4 and on the practical consideration that small sized particles are particularly prone to be swept out from the system (high β values).

D [mm]	m/A	β [-]	C_{L_2} [-]	x_{L2} [km]
5	11.575	~ 155	49.819	12.686
10	23	~ 78	35.375	17.858
20	44.851	~ 40	25.373	24.84

Table 4.1: Simulated particles' diameters and corresponding mass-to-area ratio, adimensional SRP and Jacobi constant

Taking in account the values mentioned in subsection 3.3.2, the part The propagation was set to stop in the case of two events: collision with the primary and escape from the system. The latter condition corresponds to the particle crossing the Hill sphere of the Didymos system, whose radius (~ 157 km) can be computed as of Equation 4.0.1:

$$r_{hill} = a\,(1-e)\left(\frac{m_D}{M_{sun}}\right)^{1/3} \tag{4.0.1}$$

Where a, e and m_D are respectively the semi-major axis, the eccentricity and the total mass of the binary system and M_{sun} the mass of the Sun.

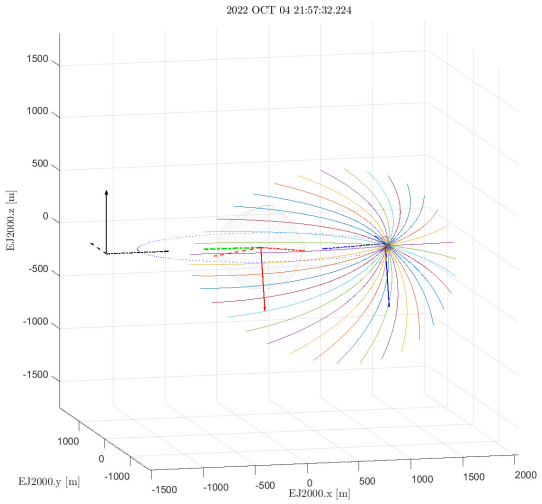

Fig. 4.2: Example of ejecta trajectories

An example of propagated trajectories is shown in Figure 4.2, in which the conical shape

set in the context of this work is also noticeable. At the end of each particle's trajectory, the Jacobi constant is computed in the AHP framework, by converting the relevant parameters to the Hill reference frame.
Following the theoretical considerations reported in subsection 3.2.2, some conclusions about the ejecta fate can be retrieved based on their energy level with respect to the equilibrium point L_2.
A first draft has been made regarding the fate of the particles in the simulation, classifying the particles as "impacted", "escaped" or "orbiting". The outcome of the analysis is summarized in Figure 4.3, where it is apparent that no particles escaped the system within the 6 hours simulated time. This was however expected, since per our settings particles with high velocities which are likely to escape in a very short time after the impact have been excluded. It is noticeable how the proportion between the orbiting and impacted particles remains the same. This is probably due to the low number of particles simulated and the various constraints applied throughout this work.

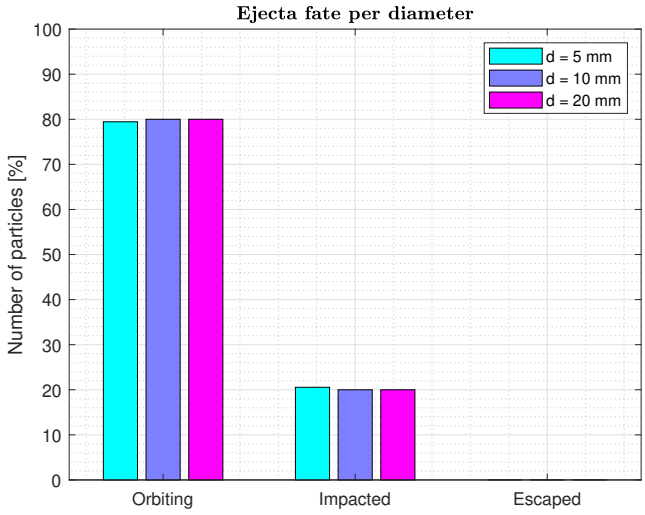

Fig. 4.3: Ejecta fate per diameter at the end of the simulated time

It is interesting to notice the time after which the impacts occur. In Figure 4.4 are shown all the times at which impacts occur. It can be observed a clear trend related to the launching direction of the particles, i.e. as the particles are launched "towards" Didymos, their impact time is fairly short, with a minimum peak of 0.5 h. Two outstanding particles belong to the d = 5 mm class, launched in a direction opposite to Didymos. It is really likely that also other particles departing from the same radial distance will impact Didymos soon, but their impact has not been covered by the simulation.

As stated, the major quantity of interest for this work is the Jacobi constant (i.e. the energy level) of the particle at the end of the trajectory, which is used to "forecast" the particles' fate according to the following criteria:

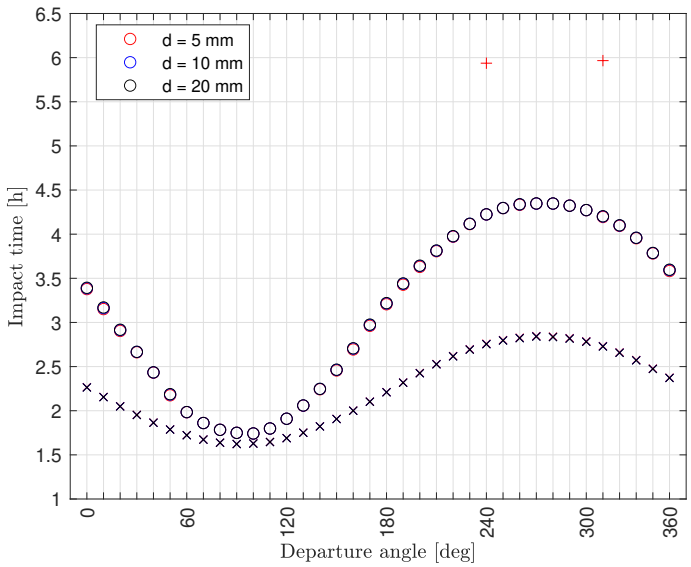

Fig. 4.4: Time at which particles impacted Didymos. Colors are shown in the legend, while the "+", "o" and "x" represents, respectively, launch positions closer and closer to the crater rim.

- if $\Gamma > \Gamma_{L2}$ and the particle is inside of the zero-velocity surface, then the particle is definitely bound to the body;
- if $\Gamma \ll \Gamma_{L2}$ the particle is a good candidate for ejection from the system;
- if $\Gamma \sim \Gamma_{L2}$ nothing can be said about the fate, however it is likely that the particle will stay in its orbit around the system for a certain amount of time and then ejected;

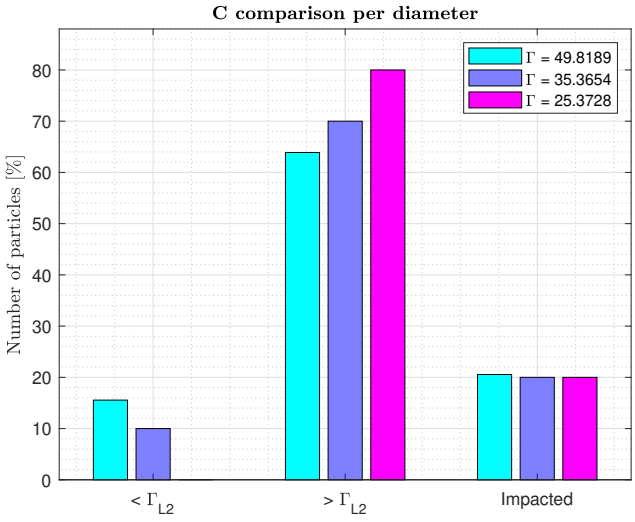

Fig. 4.5: Particles energy level with respct to the treshold set by the Jacobi constant in L2. Impacted particles are also highlighted

In Figure 4.5 is shown the outcome of the analysis on the overall sample, classifying the number of particles with respect to their energy level, i.e. if they overcome or not the

energy level set by the equilibrium point. It can be noticed that the totality of the non impacted particles with a diameter of 20 mm has an energy value that is over the reference value for that diameter, while the other two set of particles of 5 and 10 mm have respectively the 15.5 % and 10% of the non-impacted set that does not overcome the threshold.

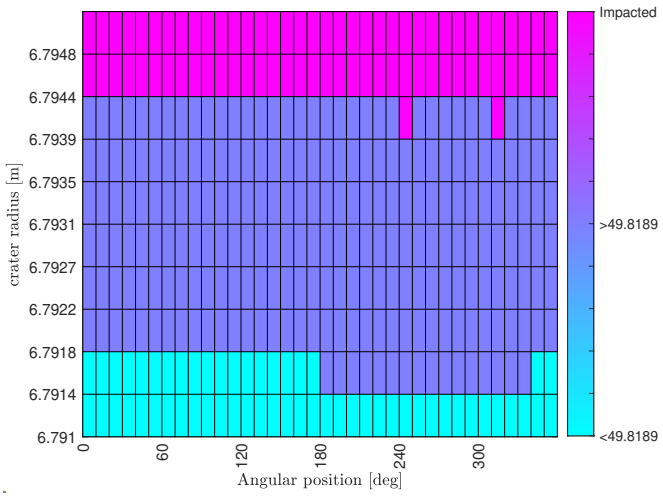

Fig. 4.6: Initial position of the particles with respect to their energy level for d = 5 mm

Another interesting outcome to be noticed is the energy level of the particles with respect to their initial position. Since the adopted initialization strategy provides an initial location of the particles in the proximity of the crater rim, it has been considered useful to visualize the aforementioned relationship by means of colored plots, one for each diameter (Figures 4.6, 4.7 and 4.8).

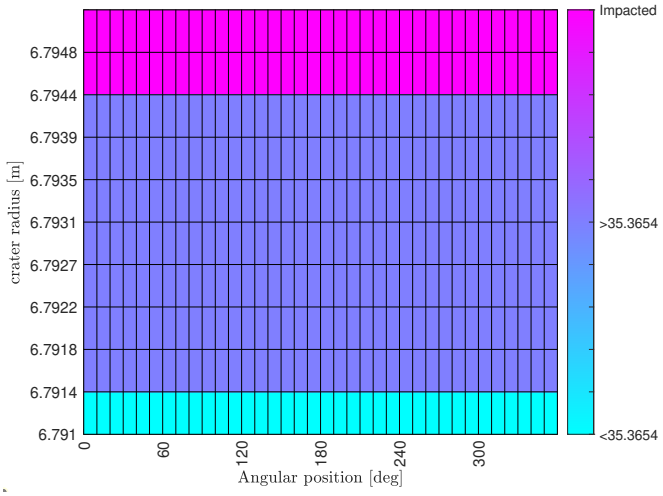

Fig. 4.7: Initial position of the particles with respect to their energy level for d = 10 mm

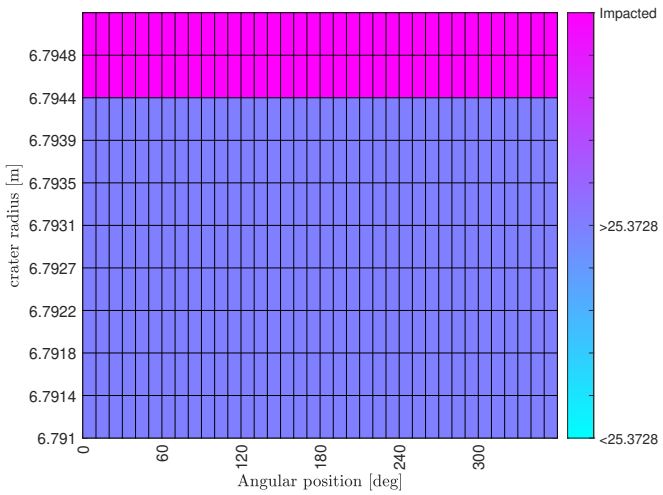

Fig. 4.8: Initial position of the particles with respect to their energy level for d = 20 mm

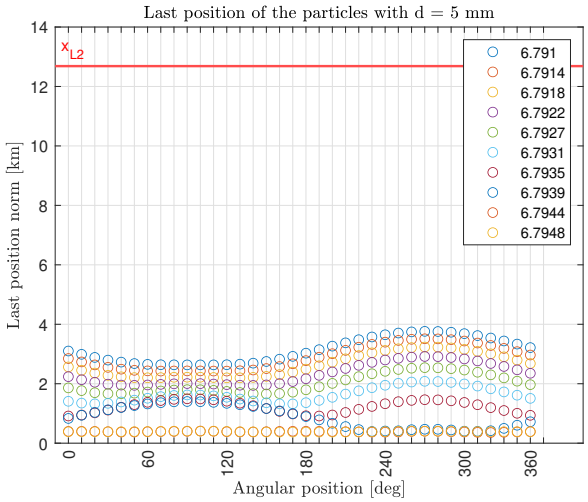

Fig. 4.9: Distance of each particle with diameter 5 mm at the end of the propagation. Red line represents the distance of L2 from the barycenter of Didymos

The x-axis represents the angular location of the particles along the i-th radius (y-axis), while the colored square represents, based on the color bar, the particles that impacted Didymos, the ones that overcome and not the energy threshold. It does seem to exist a correlation between the initial position of the particles (that in turn translates in velocity magnitude of the particles) and the energy level of the particles themselves after 6 hours. In fact, particles departing in the proximity of the crater's rim are most likely to impact, while the ones departing nearly and very far from it possess, respectively, higher and lower energy with respect to the threshold associated with their diameter. It has to be noticed that this trend is respected for particles with a diameter of 20 mm, however, as already assessed in Figure 4.3 none of them is below the Γ_{L2} threshold at the end of the simulation.

At this point, to apply our criteria it would be useful to know if the particles are inside the

ZVC. By means of a simple comparison, it turned out that the last position of each particle of the sample is currently found inside the ZVC. In fact, the distance reached by each of the particles belonging to a single diameter class is well below the distance of L2 from the system barycenter. Specifically, in Figure 4.9 is shown the conditions of particles with the smallest diameter as an example. Nevertheless, the other two diameters' follow the same trend, also taking into account that their equilibrium point distance is even higher (see Table 4.1).
Considering this outcome, the abovementioned criterion can be freely applied to all the particles. We decide here to proceed by approaching each diameter. As per the particles having a diameter of 5 mm, plotting their Jacobi constant with respect to their location on the body gives an useful insight, observing that there are quite a few particles in the region surrounding the energy level of L2 (Figure 4.10).

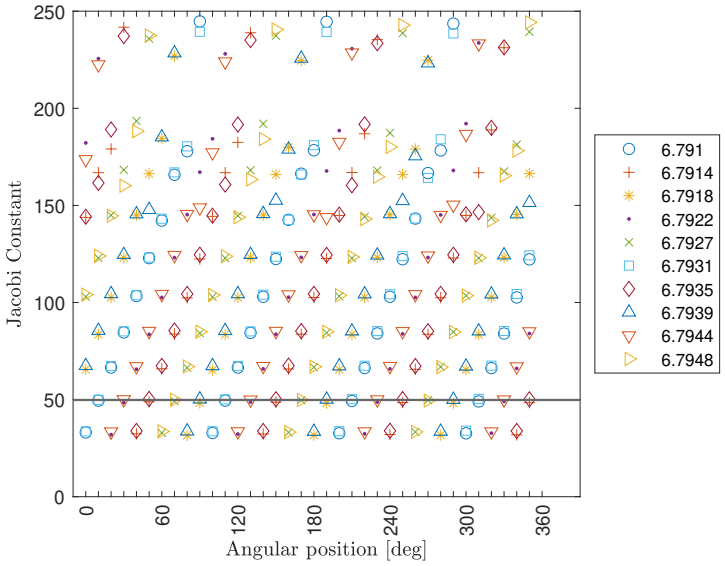

Fig. 4.10: Jacobi constant of particles with diameter 5 mm at the end of the propagation. Horizontal line represents the value of the Jacobi constant in L2.

For what concern this diameter class, it can be therefore stated that there is a number of particles that is likely-to-be ejected due to the fact that their energy level is fairly below the L2 threshold. Another part of the sample has an undecided fate and is expected to be ejected after a few orbits around Didymos. Finally, the majority of the sample is going to remain bounded to the system, due to its high energy level, and after a few orbits could be likely to impact the asteroid. Excluding the impacted particles, the outcomes are summarized in Table 4.2.

Regarding the second diameter, i.e. 10 mm, there is a portion of the sample that presents values of the Jacobi constant barely lower than the threshold (Figure 4.12), these particles have therefore undecided fate, most likely they will orbit for some time before impacting Didymos, while all the others are bounded to the system, according to the criteria defined

Bounded	LTE	N/A
80%	10%	10%

Table 4.2: Likely to escape, bounded and unassessed fate particles percentage for d = 5 mm. Impacted particles are excluded.

above.

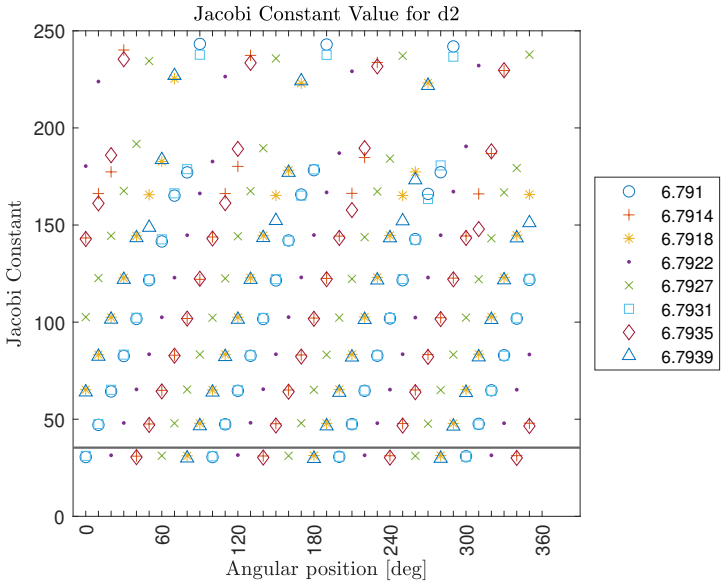

Fig. 4.11: Jacobi constant of particles with diameter 10 mm at the end of the propagation. Horizontal line represents the value of the Jacobi constant in L2.

Results are reported in Table 4.3.

Bounded	LTE	N/A
90%	0%	10%

Table 4.3: Likely to escape, bounded and unassessed fate particles percentage for d = 10 mm. Impacted particles are excluded.

About the third diameter considered, 20 mm, all the particles can be considered bounded to the system, although some of them have values of L2 very close to the Jacobi of the L2 point. A similar configuration with respect to the previous diameter applies (Figure 4.12).

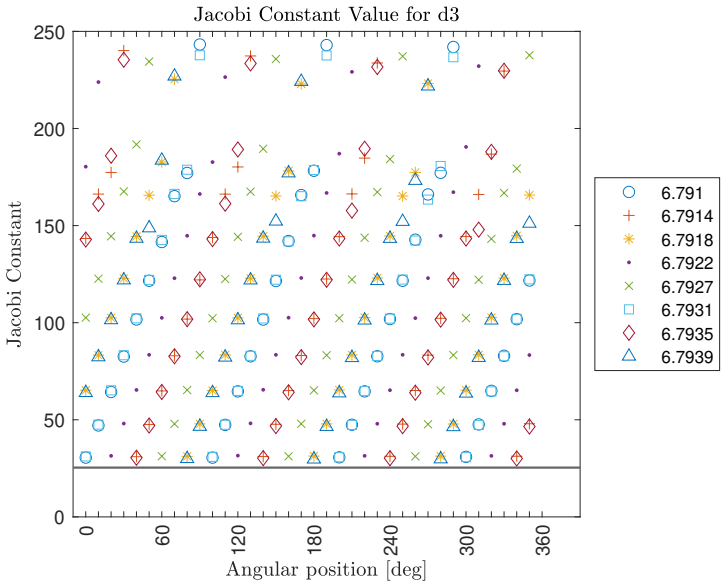

Fig. 4.12: Jacobi constant of particles with diameter 20 mm at the end of the propagation. Horizontal line represents the value of the Jacobi constant in L2.

5 | Conclusions and future developments

In this work, a novel approach has been adopted to assess the fate of ejecta particles due to the impact of the DART spacecraft on the binary asteroid 65603 Didymos. This method consists in comparing the energy level of the particles with the energy level of the equilibrium point associated to that same particle in a special three-body problem, namely the Augmented Hill Problem.

To accomplish the aforementioned, the dynamics about the asteroid has been studied and appropriate models to simulate its gravity field have been adopted. Moreover, a description of the Augmented Hill Problem has been provided, along with the model employed to simulate the cratering and the ejecta generation.

The trajectory of 1080 particles of assigned diameters (respectively D1 = 5 mm, D2 = 10 mm and D3 = 20 mm) have been propagated for 6 hours to assess their fate. Results have shown that for all the samples the percentage of impacted particles was the same, and none of them escaped the system. About the 20% of all the samples impacted Didymos, while the remaining orbiting particles fate was assessed by means of a criterion linked to their energy level with respect to the equilibrium point L2 in the Augmented Hill Problem. For the group D1, the 80% of the particles were assessed to remain bounded to the body, while another 10% is likely to escape. The remaining fate can not be assessed. For what concerns the group D2 and D3, a similar condition applies to both, given that the energy level of a 10% of the orbiting particles was really close to the L2 energy level, and so their fate in uncertain. In the D2 case, is more likely that such particles will be ejected from the system after some time. In the D3 case, instead, the particle should remain bounded to the body.

Future developments of this work are strictly linked to the approximation made. The crater location could be shifted to the real (or at least the forecasted) one, to offer a better overview on the evolution of the particles.

Moreover, to pursue the scope of this work, it has been neglected the relationship between ejection velocity and diameter as derived by the scaling laws. This choice might be either improved (e.g. by simulating more diameters) or discarded (adopting the diameters coming from the scaling laws). A good suggestion could be adopting even smaller values of particles as the sample here adopted might be improved by considering high β values as the position

of the equilibrium point L_2 approaches the body, i.e. the allowed dynamical space is reduced, and therefore a refined assessment could be made.
Another consideration is linked to the energy level. Although the results reported in this work represent a good benchmark, it has to be highlighted that the value of the Jacobi constant should be computed along the orbit, as expressed in subsection 2.2.1.
Further improvements could include the computation of periodic orbits in the AHP to assess the presence of manifolds that link the escaped particles to such trajectories.

List of Figures

List of Tables

Acronyms

AHP	Augmented Hill Problem
AIDA	Asteroid Impact and Deflection Assessment
AIM	Asteroid Impact Mission
CNSA	China National Space Administration
CR3BP	Circular Restricted Three-Boby Problem
DART	Double Asteroid Redirection Test
ESA	European Space Agency
ICE	International Cometary Explorer
JAXA	Japan Aerospace eXploration Agency
MOID	Minimum Orbit Intersection Distance
NASA	National Aeronautics and Space Administration
NEA	Near-Earth Asteroid
NEAR	Near Earth Asteroid Rendezvous
NEO	Near-Earth object
PHA	Potentially Hazardous Asteroid
SFA	Sand/Fly Ash
SRP	Solar Radiation Pressure
USSR	Union of Soviet Socialist Republics
ZVC	Zero Velocity Curves

Bibliography

[1] C. Stelzried, L. Efron, and Ellis J. Halley comet missions. NASA TDA Progress Report, 9 1986. https://ipnpr.jpl.nasa.gov/progress_report/42-87/87X.PDF.

[2] Patrick Michel, Michael Kueppers, Holger Sierks, Ian Carnelli, Andy F Cheng, Karim Mellab, Mikael Granvik, Antti Kestilä, Tomas Kohout, Karri Muinonen, et al. European component of the aida mission to a binary asteroid: Characterization and interpretation of the impact of the dart mission. *Advances in Space Research*, 62(8):2261–2272, 2018.

[3] DJ Scheeres, DD Durda, and PE Geissler. The fate of asteroid ejecta. *Asteroids III*, 1:527–544, 2002.

[4] Kevin R. Housen and Keith A. Holsapple. Ejecta from impact craters. *Icarus*, 211(1):856–875, 2011.

[5] Jennifer N Larson and G Sarid. An N-body approach to modelling debris and ejecta off small bodies: implementation and application. *Monthly Notices of the Royal Astronomical Society*, 503(1):1070–1081, 02 2021.

[6] Fabio Ferrari, Sabina D Raducan, Martin Jutzi, Eugene G Fahnestock, and Stephen R Schwartz. Dynamics of ejecta plume after the dart impact on dimorphos. In *7th IAA Planetary Defense Conference*, page 127, 2021.

[7] Tycho T Von Rosenvinge, John C Brandt, and Robert W Farquhar. The international cometary explorer mission to comet giacobini-zinner. *Science*, 232(4748):353–356, 1986.

[8] Roald Z Sagdeev, J Blamont, AA Galeev, VI Moroz, VD Shapiro, VI Shevchenko, and K Szegő. Vega spacecraft encounters with comet halley. *Nature*, 321(6067):259–262, 1986.

[9] R Reinhard. The giotto encounter with comet halley. *Nature*, 321(6067):313–318, 1986.

[10] TV Johnson, CM Yeates, and R Young. Space science reviews volume on galileo mission overview. In *The Galileo Mission*, pages 3–21. Springer, 1992.

[11] J Veverka, B Farquhar, M Robinson, P Thomas, S Murchie, A Harch, PG Antreasian,

SR Chesley, JK Miller, WM Owen, et al. The landing of the near-shoemaker spacecraft on asteroid 433 eros. *Nature*, 413(6854):390–393, 2001.

[12] Jun'ichiro Kawaguchi, Akira Fujiwara, and Tono Uesugi. Hayabusa—its technology and science accomplishment summary and hayabusa-2. *Acta Astronautica*, 62(10-11):639–647, 2008.

[13] Don Brownlee. The stardust mission: analyzing samples from the edge of the solar system. *Annual Review of Earth and Planetary Sciences*, 42:179–205, 2014.

[14] Karl-Heinz Glassmeier, Hermann Boehnhardt, Detlef Koschny, Ekkehard Kührt, and Ingo Richter. The rosetta mission: flying towards the origin of the solar system. *Space Science Reviews*, 128(1):1–21, 2007.

[15] Yuichi Tsuda, Makoto Yoshikawa, Masanao Abe, Hiroyuki Minamino, and Satoru Nakazawa. System design of the Hayabusa 2—Asteroid sample return mission to 1999 JU3. *Acta Astronautica*, 91:356–362, October 2013.

[16] DS Lauretta, SS Balram-Knutson, E Beshore, WV Boynton, C Drouet d'Aubigny, DN DellaGiustina, HL Enos, DR Golish, CW Hergenrother, ES Howell, et al. Osiris-rex: sample return from asteroid (101955) bennu. *Space Science Reviews*, 212(1):925–984, 2017.

[17] Harold F Levison, Catherine B Olkin, Keith S Noll, Simone Marchi, James F Bell III, Edward Bierhaus, Richard Binzel, William Bottke, Dan Britt, Michael Brown, et al. Lucy mission to the trojan asteroids: Science goals. *The Planetary Science Journal*, 2(5):171, 2021.

[18] X. Zhang, J. Huang, T. Wang, and Z. Huo. ZhengHe - A Mission to a Near-Earth Asteroid and a Main Belt Comet. In *50th Annual Lunar and Planetary Science Conference*, Lunar and Planetary Science Conference, page 1045, March 2019.

[19] T Arai, M Kobayashi, K Ishibashi, F Yoshida, H Kimura, K Wada, H Senshu, M Yamada, O Okudaira, T Okamoto, et al. Destiny+ mission: flyby of geminids parent asteroid (3200) phaethon and in-situ analyses of dust accreting on the earth. In *49th Annual Lunar and Planetary Science Conference*, number 2083, page 2570, 2018.

[20] A. Morbidelli, W. Jr, and Patrick Michel. Origin and evolution of near-earth objects. *Asteroids III*, 3, 01 2002.

[21] NASA JPL Center for Near Earth Objects Studies. Discovery statistics, 2022.

[22] M.J.S. Belton, C.R. Chapman, J. Veverka, K.P. Klaasen, A. Harch, R. Greeley, R. Greenberg, J.W. Head III, A. McEwen, D. Morrison, P.C. Thomas, M.E. Davies, M.H. Carr, G. Neukum, F.P. Fanale, D.R. Davis, C. Anger, P.J. Gierasch, A.P. Ingersoll, and C.B. Pilcher. First images of asteroid 243 ida. *Science*, 265(5178):1543–1547, 1994. cited By 103.

[23] William F. Bottke Patrick Michel, Francesca E. DeMeo. Asteroid systems: Binaries, triples, and pairs, 2015.

[24] J.L. Margot, M.C. Nolan, L.A.M. Benner, S.J. Ostro, R.F. Jurgens, J.D. Giorgini, M.A. Slade, and D.B. Campbell. Binary asteroids in the near-earth object population. *Science*, 296(5572):1445–1448, 2002. cited By 227.

[25] Wm. Robert Johnston. Asteroids with satellites, 2021.

[26] Amy Mainzer, J Bauer, RM Cutri, T Grav, J Masiero, R Beck, P Clarkson, T Conrow, J Dailey, P Eisenhardt, et al. Initial performance of the neowise reactivation mission. *The Astrophysical Journal*, 792(1):30, 2014.

[27] NASA. Asteroid redirect mission (arm) formulation assessment and support team (fast) final report, 2016.

[28] Jeff Foust. Nasa closing out asteroid redirect mission, 2017.

[29] Leslie McNutt, Les Johnson, Pater Kahn, Julie Castillo-Rogez, and Andreas Frick. Near-earth asteroid (nea) scout. In *AIAA Space 2014 Conference and Exposition*, page 4435, 2014.

[30] Andres Galvez, Ian Carnelli, Michael Khan, Waldemar Martens, Patrick Michel, Stephan Ulamec, and Alina Hriscu. Asteroid investigation mission: the european contribution to the aida eu-us cooperation. In *Proceedings of the 24th International Symposium on Space Flight Dynamics, Laurel, MD, USA*, 2014.

[31] Elisabetta Dotto, Vincenzo Della Corte, Marilena Amoroso, I Bertini, JR Brucato, A Capannolo, B Cotugno, G Cremonese, V Di Tana, I Gai, et al. Liciacube-the light italian cubesat for imaging of asteroids in support of the nasa dart mission towards asteroid (65803) didymos. *Planetary and Space Science*, 199:105185, 2021.

[32] Patrick Michel, Michael Küppers, and Ian Carnelli. The hera mission: European component of the esa-nasa aida mission to a binary asteroid. *42nd COSPAR Scientific Assembly*, 42:B1–1, 2018.

[33] Hannah R Goldberg, Özgür Karatekin, Birgit Ritter, Alain Herique, Paolo Tortora, Claudiu Prioroc, Borja Garcia Gutierrez, Paolo Martino, and Ian Carnelli. The juventas cubesat in support of esa's hera mission to the asteroid didymos. 2019.

[34] Fabio Ferrari, Vittorio Franzese, Mattia Pugliatti, Carmine Giordano, and Francesco Topputo. Preliminary mission profile of heraâ€™s milani cubesat. *Advances in Space Research*, 67(6):2010–2029, 2021.

[35] Yu Takahashi and DJ Scheeres. Small body surface gravity fields via spherical harmonic expansions. *Celestial Mechanics and Dynamical Astronomy*, 119(2):169–206, 2014.

[36] William Duncan MacMillan. The theory of the potential. 1958.

[37] Thomas Murray MacRobert. Spherical harmonics: an elementary treatise on harmonic functions with applications. 1947.

[38] Robert A Werner. Evaluating descent and ascent trajectories near non-spherical bodies. 2010.

[39] Marcel Brillouin. Équations aux dérivées partielles du 2e ordre. domaines à connexion multiple. fonctions sphériques non antipodes. In *Annales de l'institut Henri Poincaré*, volume 4, pages 173–206, 1933.

[40] Yu Takahashi, D. J. Scheeres, and Robert A. Werner. Surface gravity fields for asteroids and comets. *Journal of Guidance, Control, and Dynamics*, 36(2):362–374, 2013.

[41] Robert A Werner and Daniel J Scheeres. Exterior gravitation of a polyhedron derived and compared with harmonic and mascon gravitation representations of asteroid 4769 castalia. *Celestial Mechanics and Dynamical Astronomy*, 65(3):313–344, 1996.

[42] Paolo Panicucci, Benjamin Bercovici, Emmanuel Zenou, Jay McMahon, Michel Delpech, Jérémy Lebreton, and Keyvan Kanani. Uncertainties in the gravity spherical harmonics coefficients arising from a stochastic polyhedral shape. *Celestial Mechanics and Dynamical Astronomy*, 132(4):1–27, 2020.

[43] Andrea Colagrossi, Fabio Ferrari, Michèle Lavagna, Kathleen Howell, et al. Dynamical evolution about asteroids with high fidelity gravity field and perturbations modeling. In *Advances in the Astronautical Sciences (Proceedings of the AIAA/AAS Astrodynamics Specialist Conference)*, volume 156, pages 885–903, 2015.

[44] George William Hill. Researches in the lunar theory. *American journal of Mathematics*, 1(1):5–26, 1878.

[45] David A Vallado. *Fundamentals of astrodynamics and applications*, volume 12. Springer Science & Business Media, 2001.

[46] Daniel J Scheeres. *Orbital motion in strongly perturbed environments: applications to asteroid, comet and planetary satellite orbiters*. Springer, 2016.

[47] Michel Hénon. Numerical exploration of the restricted problem, v. *Astronomy and Astrophysics*, 1:223–238, 1969.

[48] K. E. PAPADAKIS. The planar photogravitational hill problem. *International Journal of Bifurcation and Chaos*, 16(06):1809–1821, 2006.

[49] Stephen B Broschart, Gregory Lantoine, and Daniel J Grebow. Quasi-terminator orbits near primitive bodies. *Celestial Mechanics and Dynamical Astronomy*, 120(2):195–215, 2014.

[50] Victory Szebehely. *Theory of orbit: The restricted problem of three Bodies*. Elsevier, 2012.

[51] Stephen B Broschart and Benjamin F Villac. Identification of non-chaotic terminator orbits near 6489 golevka. 2009.

[52] Christian Marchal. The three-body problem. 2012.

[53] K Richter and HU Keller. On the stability of dust particle orbits around cometary nuclei. *Icarus*, 114(2):355–371, 1995.

[54] DJ Scheeres and F Marzari. Temporary orbital capture of ejecta from comets and asteroids: Application to the deep impact experiment. *Astronomy and Astrophysics*, 356:747–756, 2000.

[55] Daniel J Scheeres, Steven J Ostro, RS Hudson, and Robert A Werner. Orbits close to asteroid 4769 castalia. *Icarus*, 121(1):67–87, 1996.

[56] Stefania Soldini and Yuichi Tsuda. Assessing the hazard posed by ryugu ejecta dynamics on hayabusa2 spacecraft. In *26th International Symposium of Space Flight Dynamics*, pages 1–11, 2017.

[57] Daniel Villegas-Pinto, Stefania Soldini, Yuichi Tsuda, and Jeannette Heiligers. *Temporary Capture of Asteroid Ejecta into Periodic Orbits: Application to JAXAâ€™s Hayabusa2 Impact Event.*

[58] Andrea Capannolo, Fabio Ferrari, and Michèle Lavagna. Families of bounded orbits near binary asteroid 65803 didymos. *Journal of Guidance, Control, and Dynamics*, 42(1):189–198, 2019.

[59] Yang Yu, Patrick Michel, Stephen R. Schwartz, Shantanu P. Naidu, and Lance A.M. Benner. Ejecta cloud from the aida space project kinetic impact on the secondary of a binary asteroid: I. mechanical environment and dynamical model. *Icarus*, 282:313–325, 2017.

[60] Yang Yu and Patrick Michel. Ejecta cloud from the aida space project kinetic impact on the secondary of a binary asteroid: Ii. fates and evolutionary dependencies. *Icarus*, 312:128–144, 2018.

[61] A Rossi, K Tsiganis, M Gaitanas, A Lucchetti, S Ivanovski, S Raducan, E Dotto, V Della Corte, M Amoroso, S Pirrotta, et al. Dynamics of ejecta in the didymos-dimorphos binary: Sensitivity to the system parameters. In *Lunar and Planetary Science Conference*, number 2548, page 1404, 2021.

[62] Donald E Maxwell. Simple z model for cratering, ejection, and the overturned flap. In *Impact and explosion cratering: Planetary and terrestrial implications*, pages 1003–1008, 1977.

[63] K. A. Holsapple and R. M. Schmidt. Point source solutions and coupling parameters in cratering mechanics. *Journal of Geophysical Research: Solid Earth*, 92(B7):6350–6376, 1987.

[64] K. WÃ¼nnemann, G.S. Collins, and H.J. Melosh. A strain-based porosity model for use in hydrocode simulations of impacts and implications for transient crater growth in porous targets. *Icarus*, 180(2):514–527, 2006.

[65] A. A. Amsden, H. M. Ruppel, and C. W. Hirt. Sale: a simplified ale computer program for fluid flow at all speeds. 6 1980.

[66] D Elbeshausen and K Wünnemann. isale-3d: A three-dimensional, multi-material, multi-rheology hydrocode and its applications to large-scale geodynamic processes. In *Proceedings of 11th Hypervelocity Impact Symposium (HVIS), Fraunhofer Verlag*, 2011.

[67] Katarina Miljković, Mark A Wieczorek, Gareth S Collins, Matthieu Laneuville, Gregory A Neumann, H Jay Melosh, Sean C Solomon, Roger J Phillips, David E Smith, and Maria T Zuber. Asymmetric distribution of lunar impact basins caused by variations in target properties. *Science*, 342(6159):724–726, 2013.

[68] S.D. Raducan, M. Jutzi, T.M. Davison, M.E. DeCoster, D.M. Graninger, J.M. Owen, A.M. Stickle, and G.S. Collins. Influence of the projectile geometry on the momentum transfer from a kinetic impactor and implications for the dart mission. *International Journal of Impact Engineering*, 162:104147, 2022.

[69] S.D. Raducan, T.M. Davison, and G.S. Collins. Ejecta distribution and momentum transfer from oblique impacts on asteroid surfaces. *Icarus*, 374:114793, 2022.

[70] K A Holsapple. The scaling of impact processes in planetary sciences. *Annual Review of Earth and Planetary Sciences*, 21(1):333–373, 1993.

[71] Keith A. Holsapple and Kevin R. Housen. Momentum transfer in asteroid impacts. i. theory and scaling. *Icarus*, 221(2):875–887, 2012.

[72] Giovanni Zanotti. Hypervelocity impacts on planetary bodies: Modelling craters formation and ejecta plume evolution. 2019.

[73] P Pravec, LAM Benner, MC Nolan, P Kusnirak, D Pray, JD Giorgini, RF Jurgens, SJ Ostro, J-L Margot, C Magri, et al. (65803) 1996 gt. *International Astronomical Union Circular*, 8244:2, 2003.

[74] Andrew S Rivkin, Nancy L Chabot, Angela M Stickle, Cristina A Thomas, Derek C Richardson, Olivier Barnouin, Eugene G Fahnestock, Carolyn M Ernst, Andrew F Cheng, Steven Chesley, et al. The double asteroid redirection test (dart): planetary defense investigations and requirements. *The Planetary Science Journal*, 2(5):173, 2021.

[75] ESA. Spice kernels - hera, 2022.

[76] Derek C Richardson, Olivier S Barnouin, Lance AM Benner, William Bottke, Adriano Campo Bagatin, Andrew F Cheng, Siegfried Eggl, Douglas P Hamilton, Daniel Hestroffer, Masatoshi Hirabayashi, et al. Dynamical and physical properties of 65803 didymos, the proposed aida mission target. In *AAS/Division for Planetary Sciences Meeting Abstracts# 48*, volume 48, pages 123–17, 2016.

[77] Xiyun Hou, Daniel J Scheeres, and Xiaosheng Xin. Mutual potential between two rigid bodies with arbitrary shapes and mass distributions. *Celestial Mechanics and Dynamical Astronomy*, 127(3):369–395, 2017.

[78] Alex B. Davis and Daniel J. Scheeres. High-fidelity modeling of rotationally fissioned asteroids. *The Planetary Science Journal*, 1(1):25, jun 2020.

[79] ESA. Hera spice kernel dataset, 2022.

[80] S.P. Naidu, L.A.M. Benner, M. Brozovic, M.C. Nolan, S.J. Ostro, J.L. Margot, J.D. Giorgini, T. Hirabayashi, D.J. Scheeres, P. Pravec, P. Scheirich, C. Magri, and J.S. Jao. Radar observations and a physical model of binary near-earth asteroid 65803 didymos, target of the dart mission. *Icarus*, 348:113777, 2020.

[81] Fabio Ferrari, Vittorio Franzese, Mattia Pugliatti, Carmine Giordano, and Francesco Topputo. Trajectory options for hera's milani cubesat around (65803) didymos. *The Journal of the Astronautical Sciences*, 68(4):973–994, 2021.

[82] Vladimir A Chobotov. *Orbital mechanics*. Aiaa, 2002.

[83] J. Piironen, K. Muinonen, T. Nousiainen, C. Sasse, S. Roth, and J.I. Peltoniemi. Albedo measurements on meteorite particles. *Planetary and Space Science*, 46(8):937–943, 1998.

[84] A.F. Cheng, P. Michel, M. Jutzi, A.S. Rivkin, A. Stickle, O. Barnouin, C. Ernst, J. Atchison, P. Pravec, and D.C. Richardson. Asteroid impact & deflection assessment mission: Kinetic impactor. *Planetary and Space Science*, 121:27–35, 2016.

[85] Andrew F. Cheng, Angela M. Stickle, Eugene G. Fahnestock, Elisabetta Dotto, Vincenzo Della Corte, Nancy L. Chabot, and Andy S. Rivkin. Dart mission determination of momentum transfer: Model of ejecta plume observations. *Icarus*, 352:113989, 2020.

[86] NASA. Nssdca master catalog search, 2022.

[87] Hideaki Miyamoto, Hajime Yano, Daniel J Scheeres, Shinsuke Abe, Olivier Barnouin-Jha, Andrew F Cheng, Hirohide Demura, Robert W Gaskell, Naru Hirata, Masateru Ishiguro, et al. Regolith migration and sorting on asteroid itokawa. *Science*, 316(5827):1011–1014, 2007.

[88] Esther Morrow, Daniel J Scheeres, and Dan Lubin. Solar sail orbit operations at asteroids. *Journal of Spacecraft and Rockets*, 38(2):279–286, 2001.

A | Verification and validation

In order to verify and validate the models developed for the work presented in this thesis, a series of tests were performed. This chapter explores and presents said tests together with the results.
The model developed in the context of this thesis can be seen as a combination of several submodels:

- Polyhedron Model
- Triaxial Ellipsoid
- Augmented Hill Problem
- Scaling Laws

A.1. Polyhedron model

The polyhedron model employed is the version that can be found in the HERA Spice Kernel Dataset from ESA. [79] This model, based on radar observations from the work of Naidu et al. [80], is composed of 1000 vertices and corresponding 1996 faces. As widely explained in section 2.1, the algorithm employed to simulate the gravity field is the one from Werner and Scheeres [41].
To validate the algorithm, firstly a spherical shape has been employed, by exploiting the MATLAB function `icosphere`, creating a 1280 faces polyhedron with the same mean diameter of Didymos, i.e. 780 m. (see Figure A.1a).
Then a dummy circular path at 900 m altitude from the body has been sketched in order to compare the gravity field derived by the algorithm with the field generated by a point mass. To compute the latter, it has been employed the mass value for Didymos (5.2294×10^{11} kg). The comparison of the cartesian components associated to the point mass field and polyhedron field for the sphere (Figure A.2a) shows almost identical qualitative results, as expected. Particularly, infinitesimal oscillation are found for the y component of the acceleration in the polyhedron model.

To make sure this was not a privileged condition and further validate the code, a grid of points have been generated around the body and the potential has been assessed again (Figure A.1b), this time plotting the error between each component (Figure A.2b). It can

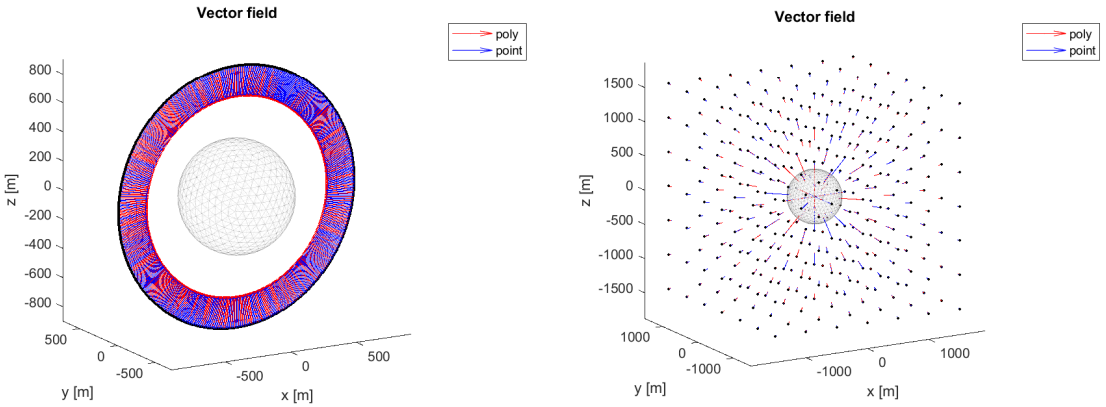

(a) Vector field associated with a dummy x-z plane circular path around a spherical polyhedron with the mean radius of Didymos A. Red arrows: polyhedral field, blue arrows: point mass field.

(b) Vector field associated with a point grid surrounding a spherical polyhedron with the mean radius of Didymos A. Red arrows: polyhedral field, blue arrows: point mass field.

Fig. A.1: Vector field representation for two different tests. Vectors are scaled of a 5×10^6 factor.

be observed how the error remains in the order of 10^{-6}.
Finally, to validate the code in the context of interest, the polyhedral model of Didymos mentioned at the beginning of this paragraph (the same plotted in other parts of this thesis and thus not shown here) was included in the code, computing the gravity field for the same circular path of the spherical case. Once again, the results are reported in Figure A.3. The order of magnitude of the error gives a final insight on the correctness of the code.

A.2. Triaxial ellipsoid model

The shape adopted for Dimorphos corresponds to a triaxial ellipsoid with axes of 103, 77 and 69 meters respectively. To test the triaxial ellipsoid algorithm implemented, a simple verification has been conducted by working with a nearly spherical shape (a = 103, b = 102 and c = 101) due to the validity of the model for $a > b > c$. So a dummy circular xy path has been sketched and the potential has been computed both by making use of the point mass formulation and the ellipsoid model. In this case the point mass formulation reads:

$$\mathbf{a} = -\frac{4}{3}\pi G \rho abc \frac{\mathbf{r}}{r^3}$$

The setup and the results are reported respectively in Figure A.4 and Figure A.5. It can be observed that the error does not exceed 10^{-7}, which serves as a confirmation for the validity of the model.

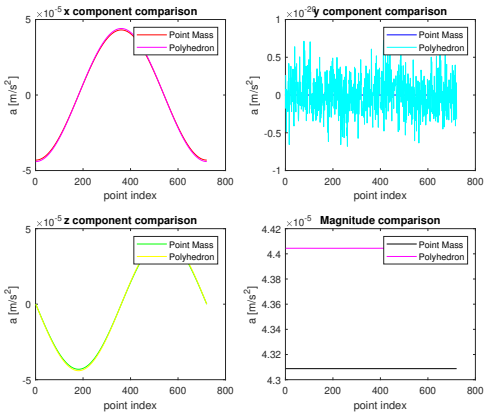

(a) Comparison of the polyhedral and point mass acceleration in terms of x,y,z components and magnitude in the case of circular xz path.

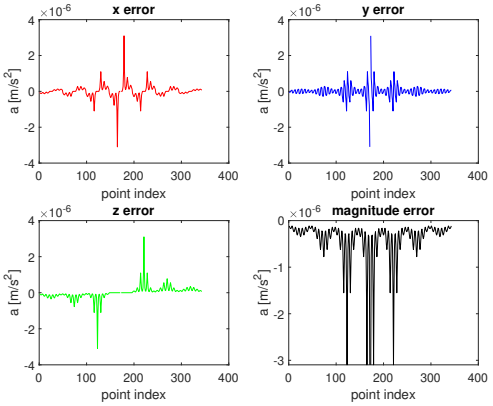

(b) Error between the polyhedral and point mass acceleration in terms of x,y,z components and magnitude in the case of points grid surrounding the body.

Fig. A.2: Comparison between polyhedral and point mass gravity fields

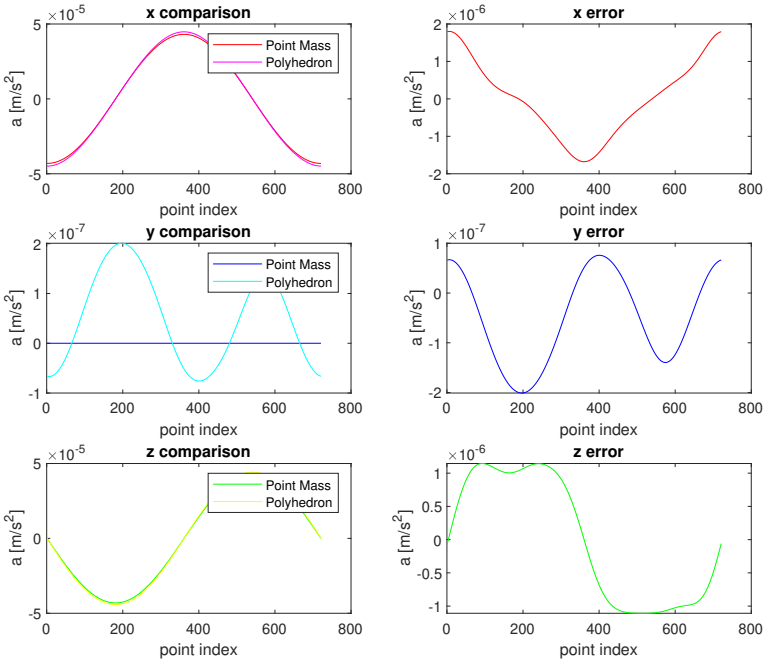

Fig. A.3: Left column (right column): comparison (error) of the polyhedral and point mass acceleration in terms of x,y,z components and magnitude using Didymos A polyhedral shape and a circular xz path.

A.3. Augmented Hill Problem

The Augmented Hill Problem point mainly refers to the correctness of the propagated trajectory, namely the solution of the ODEs associated to the problem making use of a `ode113` solver - adaptive step-size Runge-Kutta Dormand-Price integrator -. The relative

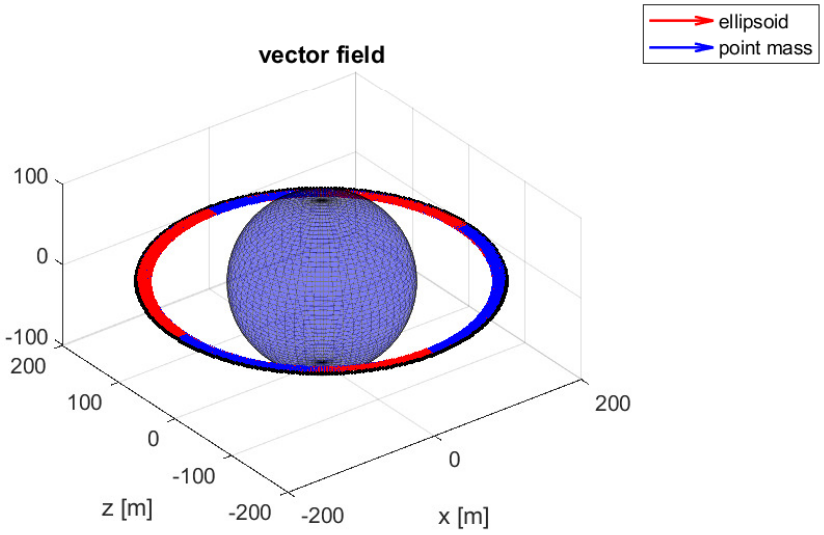

Fig. A.4: Vector field associated with a dummy circular orbit around a nearly-spherical object with size 103 - 102 - 101 m. Red arrows: ellipsoid field, blue arrows: point mass field.

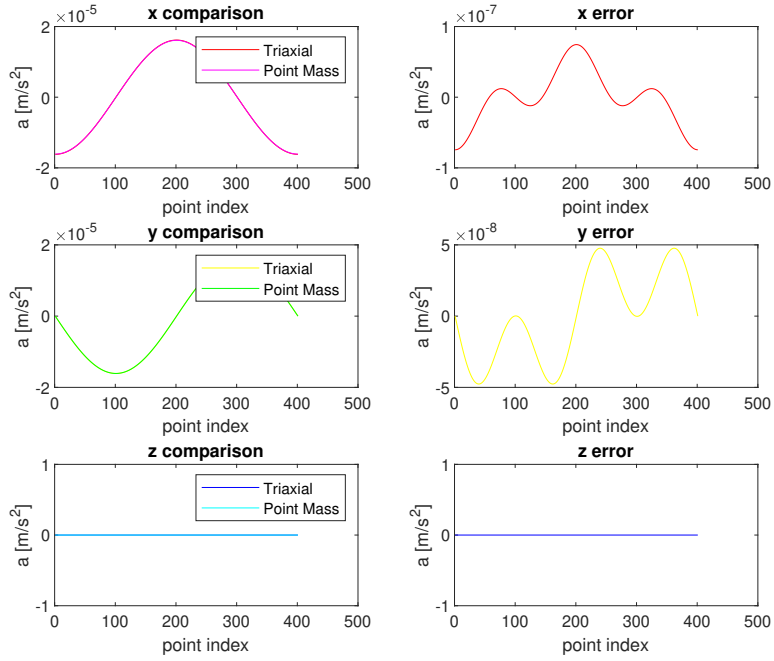

Fig. A.5: Left column (right column): comparison (error) of the ellipsoid (103,102,101) and point mass acceleration in terms of x,y,z components

and absolute error tolerances are both set to 10^{-13}, close to the minimum allowed by the integrator. As mentioned in the body of this thesis, because the AHP model is time-

invariant, it admits an energy integral, which is formally known as the Jacobi constant, C. Therefore, in an ideal computation, the value of C must remain constant along any trajectory in the AHP [45]. Due to numerical fluctuations however this number is always different from zero, although remaining very close to it. To test the formulation of the differential problem, we choose some known trajectories to be integrated and we check the maximum deviation of the Jacobi constant from zero along the orbit. For the sake of completeness, both orbits with and without SRP have been considered. Initial conditions for such orbits have been taken from [57], therefore data provided for asteroid Ryugu (Figure A.6) are used for the tests, unless specified otherwise.

	Asteroid axes [m]						
μ [m^3 s^{-2}]	a	b	c	Avg. radius, R_a [m]	Orb. period, T_a [days]	Density, ρ [kg/m^3]	C_R
32	446.5	439.7	433.9	440	473.889287	1270	0.07

Fig. A.6: Asteroid Ryugu data for the AHP

Before computing the orbits, to additionally check the correctness of the code, we computed the variation of the equilibrium points location with respect to the adimensional SRP value and compared the qualitative outcome with the result obtained in [57]. The comparison is shown in Figure A.7. The same comparison was performed for the Zero Velocity Curves of the problem for two different values of SRP. The outcome is shown in figure Figure A.8.

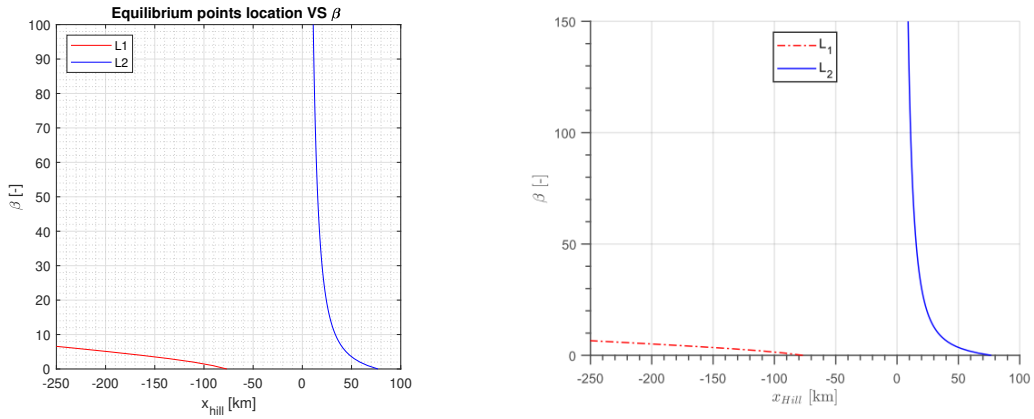

(a) L1 and L2 location VS SRP *(b) L1 and L2 location VS SRP*

Fig. A.7: Equilibrium points location with respect to SRP, comparison of this work's results (left) and [57] (right) for the asteroid Ryugu

For what concerns the orbit integration and the maximum error on the Jacobi constant (namely ΔC_{max}), it has been found that errors by using the `ode45` integrator were much wider of the ones using the `ode113` . In the first case, the results were not coincident with the one obtained in [57], and since the qualitative plot of the orbit was found to be equal, it is reasonable thinking that this discrepancy depends upon the machine used. Given

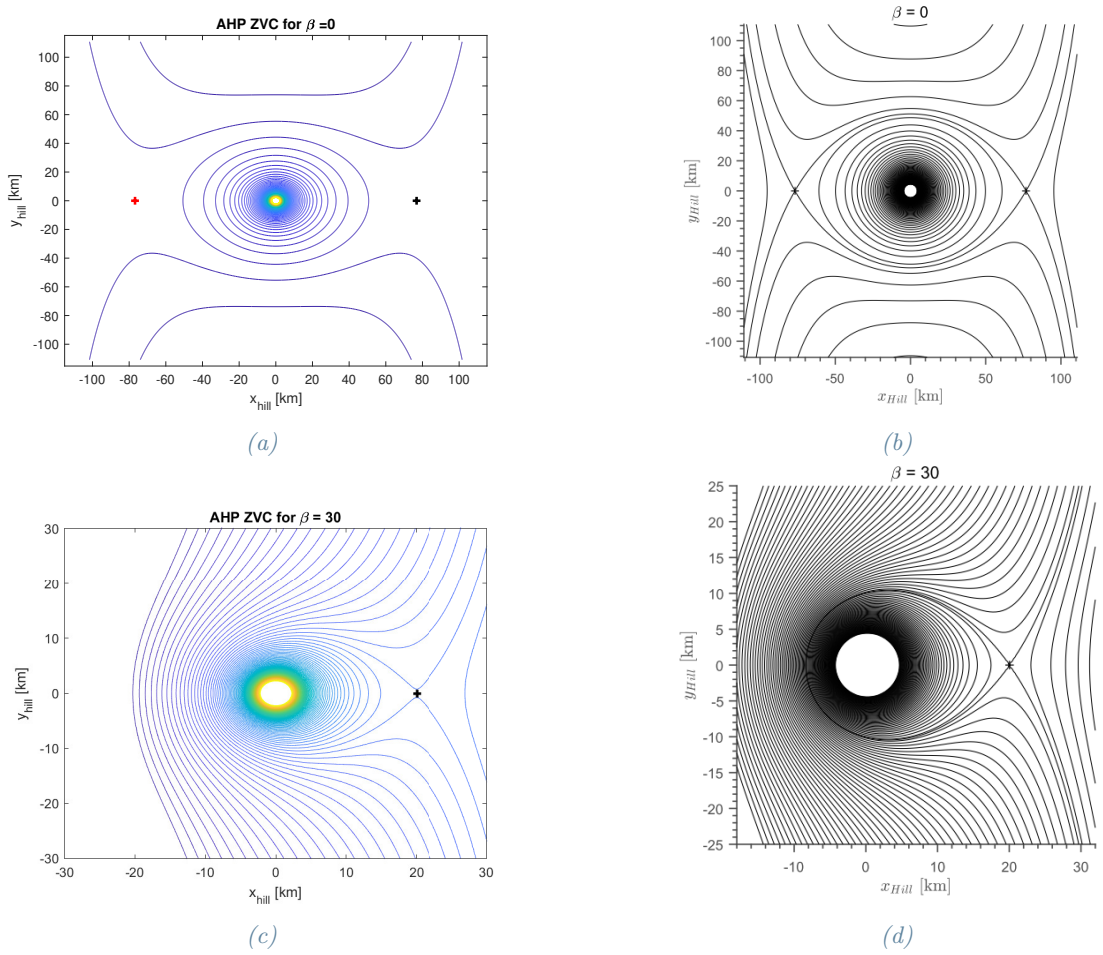

Fig. A.8: ZVC as obtained in this validation (left) and from [57] (right) for different values of adimensional SRP. In figure a and c the red and black crosses represent the equilibria points location. It can be noticed how L1 shift towards the Sun as the radiation pressure increases

that, the computation of the maximum error on the Jacobi constant have been performed using a `ode113` integrator. The results are reported in Table A.1. It can be observed that the error value never exceeds 10^{-10} that is considered a sufficient condition for the work carried on in this thesis.

β	Family	$\Delta C_{\max}$	$x_0[-]$	$z_0[-]$	$\dot{y}_0[-]$	$\dot{z}_0[-]$	$t[-]$
0	a	$1.4356516 \times 10^{-11}$	0.32125800	0	2.08969372	0	3.56886117
100	a	$3.044320351 \times 10^{-11}$	0.07112700	0	3.63083747	0	0.17727777
0	g'	$8.0420115 \times 10^{-11}$	0.25546700	0	2.50181945	0	4.73721046
100	g'	$2.540367916 \times 10^{-10}$	0.06333400	0	4.18020864	0	0.18556618
0	terminator	$1.19095844 \times 10^{-11}$	0.30433087	0.34000788	1.48923206	0	2.97697355
100	terminator	$4.56878979 \times 10^{-12}$	0.08519857	0.04001235	1.39565598	0	0.18390886

Table A.1: Initial conditions as provided by [57]. The column of the error has been modified with the values obtained in this work for each of the orbits. Values of initial y position and x velocity are always null and therefore excluded from the table

To further validate the code, a qualitative comparison of the orbit plotted in [88] around

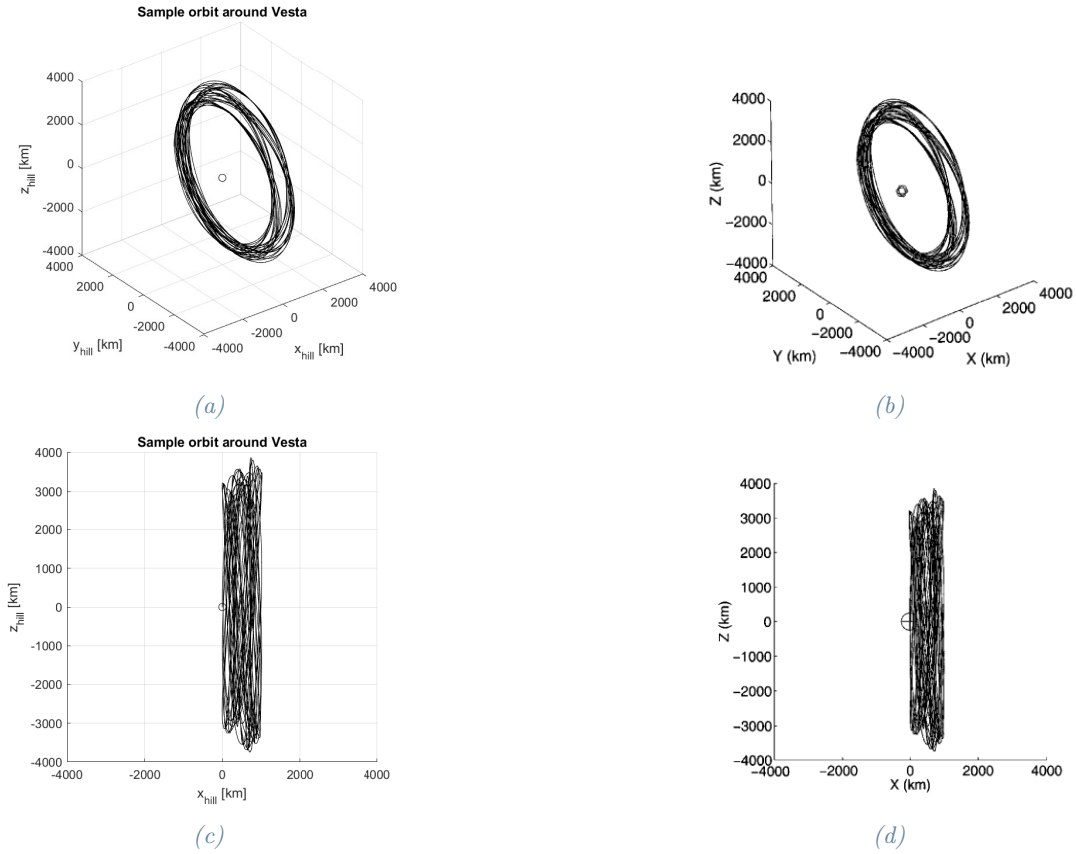

Fig. A.9: Qualitative validation of the Hill problem code, integration of an orbit around Vesta with parameters provided by [88]. Left column: integration of this work, right column: courtesy of [88]

Vesta has been made. In this case the Hill problem data have been changed accordingly, modifying the gravity parameter and the solar radiation pressure value. The result of the integration compared with the original work is reported in Figure A.9

A.4. Scaling Laws

The scaling laws as proposed by [59] have been reproduced here to assess the validity of the implemented code for the initialization of the ejecta. Using the same parameters, it has been retrieved that the total mass of the ejecta for the size ranges specified (from 0.1 to 100 mm) is in the same order of magnitude of that proposed by the authors of the paper (see Table A.2).

D_1 [m]	D_2 [m]	N_{part}	N_{part} (from [59])
0.01	0.1	3.4601×10^7	3.44×10^7
0.001	0.01	2.1832×10^{10}	2.17×10^{10}
0.0001	0.001	1.3775×10^{13}	1.37×10^{13}

Table A.2: Comparison between the number of particles obtained by Yu et al. and in this work for the scaling laws

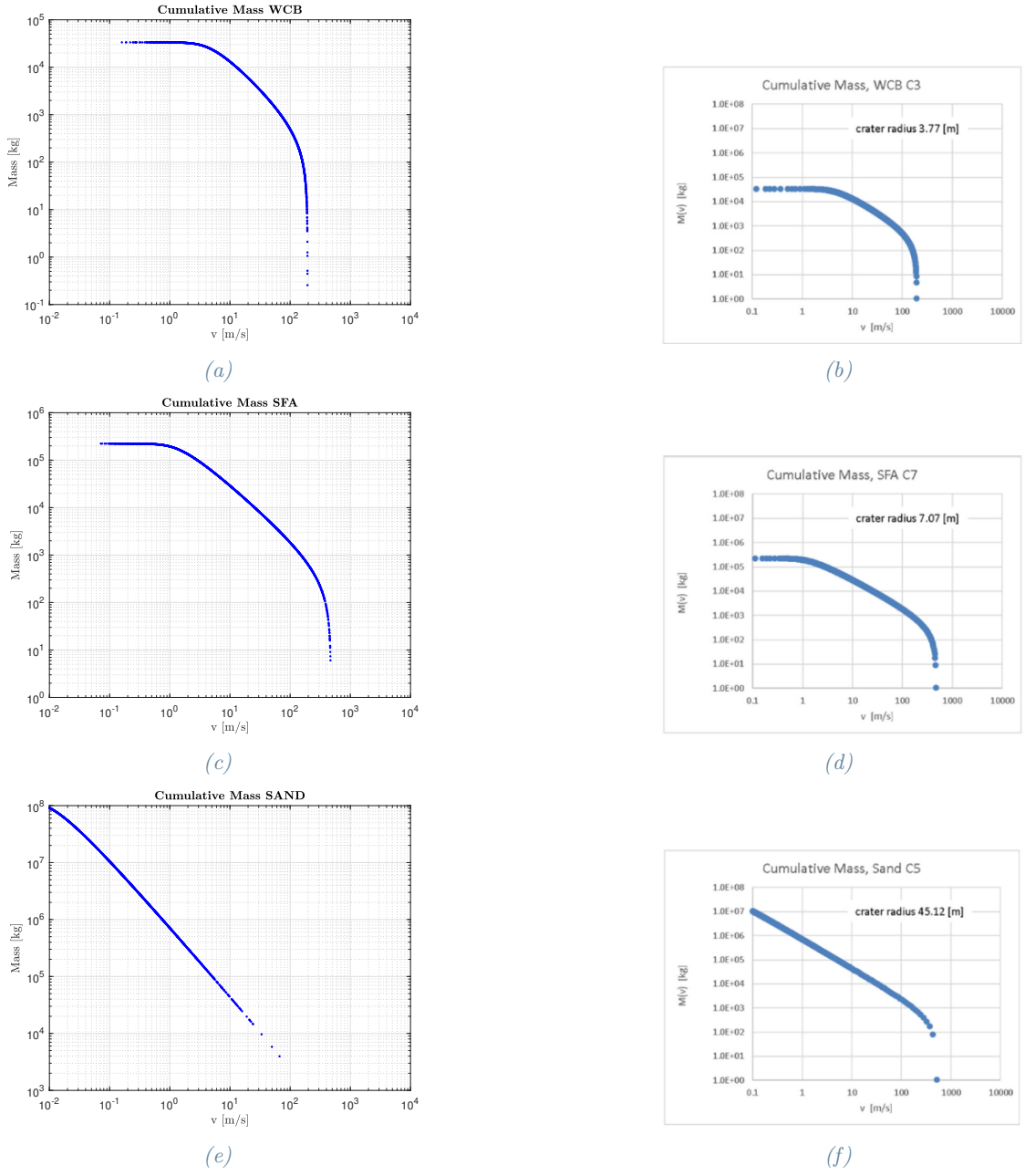

Fig. A.10: Qualitative validation of the Scaling Laws for different materials. Images on the right are from [85]

Another deeper verification has been made by reproducing some of the results from Cheng et al. [85], that compared the outcome of the DART impact for different materials. Hereby, employing the same parameters, it has been computed the radius of the crater and the mass distribution vs the velocity for three different materials, i.e. Weakly Cemented Basalt, Sand/Fly Ash and Sand. The comparison of the obtained crater radius is reported in Table A.3.

It can be noticed a discrepancy between the crater radius in the SAND case: this should

Material	Estimated CR [m]	CR from Cheng [m]
WCB	3.7718	3.77
SFA	7.0776	7.07
SAND	44.5254	45.12

Table A.3: Comparison between the crater radius estimated with the code employed in this thesis and the results from [85]

be due to a different estimate of the surface gravity of Dimorphos (i.e. the g) that appears in the expression for the radius, being an impact with sand usually gravity driven. A qualitative yet significant confrontation of the plots for the mass distribution with respect to the velocity from the same paper are reported in Figure A.10.